

Revisiting the Galaxy Shape and Spin Alignments with the Large-Scale Tidal Field: An Effective Practical Model

Jounghun Lee

*Astronomy Program, Department of Physics and Astronomy, Seoul National University,
Seoul 08826, Republic of Korea*

jounghun@astro.snu.ac.kr

ABSTRACT

An effective practical model with two characteristic parameters is presented to describe both of the tidally induced shape and spin alignments of the galactic halos with the large-scale tidal fields. We test this model against the numerical results obtained from the Small MultiDark Planck simulation on the galactic mass scale of $0.5 \leq M/(10^{11} h^{-1} M_{\odot}) \leq 50$ at redshift $z = 0$. Determining empirically the parameters from the numerical data, we demonstrate how successfully our model describes simultaneously and consistently the amplitudes and behaviors of the probability density functions of three coordinates of the shape and spin vectors in the principal frame of the large scale tidal field. Dividing the samples of the galactic halos into multiple subsamples in four different mass ranges and four different types of the cosmic web, and also varying the smoothing scale of the tidal field from $5 h^{-1}\text{Mpc}$ to 10, 20, $30 h^{-1}\text{Mpc}$, we perform repeatedly the numerical tests with each subsample at each scale. Our model is found to match well the numerical results for all of the cases of the mass range, smoothing scale and web type and to properly capture the scale and web dependence of the spin flip phenomenon.

Subject headings: cosmology:theory — large-scale structure of universe

1. Introduction

The physical properties of the observed galaxies in the universe is a reservoir of information on the conditions under which they formed, the evolutionary processes which they went through, and the interactions in which they are involved. Although the local conditions and processes at the galactic scales must have had the most dominant impact on the galaxies,

the non-local effects beyond the galactic scales are also believed to have contributed partly to their physical properties (e.g., Pandey & Sarkar 2017). Subdominant as its contribution is, the non-local effects on the galaxies are worth investigating, since it may contain valuable independent information on the galaxy formation and the background cosmology as well.

The non-local effects on the galaxies are manifested by the correlations between the galaxy properties and the large-scale environments. Among various properties of the galaxies that have been found correlated with the large-scale environments, the shape and spin alignments of the galaxies with the large-scale structures (collectively called the galaxy intrinsic alignments) have lately drawn considerable attentions, inspiring vigorous extensive studies (see Joachimi et al. 2015; Kiessling et al. 2015; Kirk et al. 2015, for recent reviews). It is partially because the galaxy intrinsic alignments, if present and significant, could become another systematics in the measurements of the extrinsic counterparts caused by the weak gravitational lensing (see Troxel & Ishak 2015, and references therein). The other important motivation for the recent flurry of research on this topic is that the origin of the galaxy intrinsic alignments is amenable to the first order perturbation theory and thus a rather fundamental approach to this topic is feasible (e.g., Heavens et al. 2000; Lee & Pen 2000; Catelan et al. 2001; Crittenden et al. 2001; Lee & Pen 2001; Porciani et al. 2002; Hui & Zhang 2008; Blazek et al. 2011, 2015; Tugendhat & Schäfer 2018).

In the first order Lagrangian perturbation theory (Zel’dovich 1970; Buchert 1992), the minor (major) eigenvectors of the inertia momentum tensors of the proto-galactic regions are perfectly aligned with the major (minor) eigenvectors of the local tidal tensors around the regions. Several N -body simulations have indeed detected the existence of strong correlations between the inertia momentum and local tidal tensors at the proto-galactic sites (Lee & Pen 2000; Porciani et al. 2002; Lee et al. 2009). Since the tidal fields smoothed on different scales are cross correlated, the eigenvectors of the inertia momentum tensors of the proto-galactic regions are expected to be aligned with those of the large-scale tidal fields. The major eigenvectors of the inertia momentum tensors of the proto-galaxies correspond to the most elongated axes of their shapes, while the minor eigenvectors of the large-scale tidal tensors correspond to the directions along which the surrounding matter become minimally compressed. Henceforth, this expectation based on the first order Lagrangian perturbation theory basically translates into the possible alignments between the galaxy shapes and the most elongated axes of the large-scale structures such as the axes of the filaments, the signals of which have been detected by several numerical and observational studies (e.g., Altay et al. 2006; Hahn et al. 2007b; Zhang, Yang & Faltenbacher 2009; Zhang et al. 2013; Chen et al. 2016, and references therein).

In the linear tidal torque (LTT) theory that Doroshkevich (1970) formulated by com-

binning the first order Lagrangian perturbation theory with the Zel’dovich approximation (Zel’dovich 1970), the anisotropic tidal field of the surrounding matter distribution originates the spin angular momentum of a proto-galaxy provided that its shape departs from a spherical symmetry. The generic and unique prediction of this LTT theory is the inclinations of the spin vectors of the proto-galaxies toward the intermediate eigenvectors of the large scale tidal field (Lee & Pen 2000), which has also garnered several numerical and observational supports (e.g., Navarro et al. 2004; Trujillo et al. 2006; Hahn et al. 2007a; Lee & Erdogdu 2007; Wang et al. 2011; Zhang et al. 2015; Chen et al. 2016).

The recently available large high-resolution N -body simulations that covered a broad mass range, however, limited the validity of the LTT prediction to the mass scale of $M \geq M_t \sim 10^{12} h^{-1} M_\odot$, showing that on the mass scale below M_t the spin vectors of dark matter halos at $z = 0$ are aligned not with the intermediate but rather with the minor eigenvectors of the large scale tidal field, similar to the axes of the halo shapes (Aragón-Calvo et al. 2007; Hahn et al. 2007b; Paz et al. 2008; Zhang, Yang & Faltenbacher 2009; Codis et al. 2012; Libeskind et al. 2013; Trowland et al. 2013; Dubois et al. 2014; Veena et al. 2018). This difference in the spin alignment tendency between the low and high mass scales were found most conspicuous in the filament environments: the spin axes of the galactic halos with masses lower (higher) than M_t measured at $z = 0$ tend to be parallel (perpendicular) to the elongated axes of their host filaments, in contradiction with the LTT prediction. The transition of the spin alignment tendency at M_t is often called ”spin flip” phenomenon (Codis et al. 2012) and the break-down of the LTT prediction below M_t has also been witnessed in recent observations (Tempel et al. 2013; Tempel & Libeskind 2013; Hirv et al. 2017; Chen et al. 2018).

The detection of this spin-flip phenomenon puzzled the community and urged it to find a proper answer to the critical question of what the origin of this phenomenon is. What has so far been suggested as a possible origin includes the major merging events, mass dependence of the merging and accretion processes, assembly bias, vorticity generation inside filaments, web-dependence of the galaxy formation epochs, nonlinear tidal interactions, geometrical properties of the host filaments and etc (Bett & Frenk 2012; Lacerna & Padilla 2012; Codis et al. 2012; Libeskind et al. 2013; Welker et al. 2014; Codis et al. 2015; Laigle et al. 2015; Bett & Frenk 2016; Wang & Kang 2017; Veena et al. 2018). Although these previously suggested factors were believed to play some roles for the occurrence of the spin-flip phenomenon, none of them are fully satisfactory in explaining all aspects of the spin-flip phenomenon including the dependence of the transition mass scale M_t on the types of the cosmic web, redshifts, and scales of the filaments.

The occurrence of the spin-flip phenomenon basically implies that for the case of the

galaxies with masses $M \leq M_t$, the tendency of the spin alignments with the large scale tidal field becomes similar to that of the shape alignments. Thus, it is suspected that whatever caused the spin-flip phenomenon, it should be linked to the shape alignments with the large scale tidal field. To address these remaining issues, what is highly desired is an effective model that can describe consistently and simultaneously both of the galaxy shape and spin alignments. Here, we attempt to construct such a model by modifying the original LTT theory and to explore if the shapes of the galaxies also show any transition of the alignment tendency like the spin counterparts

The organization of this Paper is as follows. A refined analytic model for the galaxy shape alignments is presented in Section 2.1 and tested against the numerical results in Section 2.2. An effective model for the tidally induced spin alignments is presented in Section 3.1 and tested against the numerical results in Section 3.2. A discussion over the possible application of this model as well as a summary of the results is presented in Section 4. Throughout this Paper, we will assume a Planck universe whose total energy density is dominantly contributed by the cosmological constant (Λ) and the cold dark matter (CDM) (Planck Collaboration et al. 2014).

2. Tidally Induced Shape Alignments

2.1. An Analytic Model

Suppose a galactic halo located in a region where a tidal tensor \mathbf{T} has its major, intermediate and minor eigenvectors ($\hat{\mathbf{u}}_1$, $\hat{\mathbf{u}}_2$ and $\hat{\mathbf{u}}_3$, respectively), corresponding to the largest, second to the largest, smallest eigenvalues (λ_1 , λ_2 and λ_3 , respectively). The tidal tensor \mathbf{T} depends on the smoothing scale, R_f , as $\mathbf{T}(\mathbf{x}) \propto \partial_i \partial_j \int d\mathbf{x}' \Phi(\mathbf{x}') W(|\mathbf{x} - \mathbf{x}'|; R_f)$, where $\Phi(\mathbf{x})$ is the perturbation potential field and $W(|\mathbf{x} - \mathbf{x}'|; R_f)$ is a window function with a filtering radius R_f . In the current analysis, we adopt a Gaussian window function.

As mentioned in Section 1, the first order Lagrangian perturbation theory (Zel'dovich 1970; Buchert 1992) predicts a strong anti-correlation between the principal axes of the inertia momentum tensor of a galactic halo and the local tidal tensor in the Lagrangian regime. According to this theory, the correlation between the two tensors is strongest if the two tensors are defined on the same scale (i.e., the virial radius of the halo, R_g), becomes weaker if R_f is larger than R_g . If the shape of this galactic halo can be approximated by an ellipsoid, then the direction of the coordinate vector of the largest shape ellipsoid, $\mathbf{e} = (e_1, e_2, e_3)$ (i.e., the major principal axis of the inertia momentum tensor) is expected to be aligned with $\hat{\mathbf{u}}_3$ (i.e., the minor principal axis of the local tidal tensor) along which the

surrounding matter is least compressed, provided that $\lambda_1 \neq \lambda_2 \neq \lambda_3$.

This alignment tendency can be statistically quantified by the conditional joint probability density function of three coordinates of the largest shape ellipsoid axis, $p(e_1, e_2, e_3|\hat{\mathbf{T}})$, where $\hat{\mathbf{T}}$ is a unit *traceless* tidal tensor defined as $\hat{\mathbf{T}} \equiv (\mathbf{T} - \text{Tr}(\mathbf{T})/3)/|\mathbf{T} - \text{Tr}(\mathbf{T})/3|$ with $\text{Tr}(\mathbf{T})$ denoting the trace of \mathbf{T} . As Lee & Pen (2001) and Lee (2004) did, we assume here that $p(e_1, e_2, e_3|\hat{\mathbf{T}})$ follows a multivariate Gaussian distribution of

$$p(e_1, e_2, e_3|\hat{\mathbf{T}}) = \frac{1}{[(2\pi)^3 \det(\boldsymbol{\Sigma})]^{1/2}} \exp \left[-\frac{1}{2} (\mathbf{e} \cdot \boldsymbol{\Sigma}^{-1} \cdot \mathbf{e}) \right], \quad (1)$$

where the components of the covariance matrix, $\boldsymbol{\Sigma} = (\Sigma_{ij})$, are defined as the conditional ensemble averages, $\Sigma_{ij} \equiv \langle e_i e_j | \hat{\mathbf{T}} \rangle$. Here, we suggest the following practical formula for $\langle e_i e_j | \hat{\mathbf{T}} \rangle$:

$$\langle e_i e_j | \hat{\mathbf{T}} \rangle = \frac{1 + d_t}{3} \delta_{ij} - d_t \hat{T}_{ij}, \quad (2)$$

where d_t is the shape correlation parameter that measures the alignment strength between \mathbf{e} and $\hat{\mathbf{u}}_3$. Note that this formula describes a linear dependence of the covariance, $\langle e_i e_j | \hat{\mathbf{T}} \rangle$, on \mathbf{T} (Catelan et al. 2001; Lee & Pen 2008; Hui & Zhang 2008), unlike a spin vector whose covariance has a quadratic dependence on \mathbf{T} (White 1984; Lee & Pen 2000, 2001).

Focusing only on the direction of \mathbf{e} , we marginalize $p(e_1, e_2, e_3|\mathbf{T})$ over $e \equiv |\mathbf{e}|$ to have

$$\begin{aligned} p(\hat{\mathbf{e}}|\hat{\mathbf{T}}) &= \int p(\mathbf{e}|\hat{\mathbf{T}}) e^2 de \\ &= \frac{1}{4\pi \det(\boldsymbol{\Sigma})^{1/2}} (\hat{\mathbf{e}} \cdot \boldsymbol{\Sigma}^{-1} \cdot \hat{\mathbf{e}})^{-3/2}, \end{aligned} \quad (3)$$

where $\hat{\mathbf{e}} \equiv \mathbf{e}/e$ denotes the unit vector in the direction of the largest shape ellipsoid axis. While $\hat{\mathbf{T}}$ shares the same orthonormal eigenvectors with \mathbf{T} , its eigenvalues, $\hat{\lambda}_1, \hat{\lambda}_2, \hat{\lambda}_3$, are subject to two additional constraints of $\sum_{i=1}^3 \hat{\lambda}_i = 0$ and $\sum_{i=1}^3 \hat{\lambda}_i^3 = 1$ (Lee & Pen 2001).

Putting Equation (2) into Equation (3) leads to the following analytic expression

$$p(\hat{\mathbf{e}}|\hat{\mathbf{T}}) = \frac{1}{2\pi} \left[\prod_{n=1}^3 (1 + d_t - 3d_t \hat{\lambda}_n) \right]^{-\frac{1}{2}} \left(\sum_{l=1}^3 \frac{|\hat{\mathbf{u}}_l \cdot \hat{\mathbf{e}}|}{1 + d_t - 3d_t \hat{\lambda}_l} \right)^{-\frac{3}{2}}, \quad (4)$$

since $\hat{T}_{ij} = \hat{\lambda}_i \delta_{ij}$ in the principal axis frame of $\hat{\mathbf{T}}$. Now, the conditional probability density function, $p(|\hat{\mathbf{u}}_i \cdot \hat{\mathbf{e}}|)$, for $i \in \{1, 2, 3\}$, can be obtained as

$$p(|\hat{\mathbf{u}}_i \cdot \hat{\mathbf{e}}|) = \int_0^{2\pi} p(\hat{\mathbf{e}}|\hat{\mathbf{T}}) d\phi_{jk}, \quad (5)$$

where ϕ_{jk} is the azimuthal angle of $\hat{\mathbf{e}}$ in the plane spanned by $\hat{\mathbf{u}}_j$ and $\hat{\mathbf{u}}_k$ perpendicular to $\hat{\mathbf{u}}_i$.

Equation (4) indicates that the completion of this analytic model requires us to determine the value of d_t . If $\hat{\mathbf{e}}$ is perfectly aligned with $\hat{\mathbf{u}}_3$, then d_t would be unity. Whereas, the zero value of d_t would correspond to the case that $\hat{\mathbf{e}}$ is completely random having no correlation with $\hat{\mathbf{u}}_3$. As done in Lee & Pen (2001), for the determination of d_t , we first evaluate the conditional ensemble average, $\langle \hat{e}_i \hat{e}_j | \hat{\mathbf{T}} \rangle$, under the assumption of $d_t \ll 1$

$$\langle \hat{e}_i \hat{e}_j | \hat{\mathbf{T}} \rangle = \int \hat{e}_i \hat{e}_j p(\hat{\mathbf{e}} | \hat{\mathbf{T}}) d\hat{\mathbf{e}}, \quad (6)$$

$$\approx \left[\left(\frac{1}{3} + \frac{3}{5} d_t \right) - \frac{3}{5} d_t \hat{\lambda}_i \right] \delta_{ij}, \quad (7)$$

Note that the off-diagonal elements vanish in Equation (7) since $\hat{T}_{ij} = \hat{\lambda}_i \delta_{ij}$ in its principal frame. Multiplying Equation (7) by $\hat{\lambda}_i$ and summing over the three components, we finally derive a simple analytic formula for d_t :

$$d_t = -\frac{5}{3} \sum_{i=1}^3 \hat{\lambda}_i \langle \hat{e}_i^2 | \hat{\mathbf{T}} \rangle. \quad (8)$$

The constraints of $\sum_{i=1}^3 \hat{\lambda}_i = 0$ and $\sum_{i=1}^3 \hat{\lambda}_i^2 = 1$ are used to derive the above formula. Equation (8) implies that once the values of $\hat{\lambda}_i$ and $\langle \hat{e}_i^2 | \hat{\mathbf{T}} \rangle$ are measured, the shape correlation parameter, d_t , can be empirically determined.

It is worth recalling that the shape correlation parameter, d_t , depends on the smoothing scale, R_f . It is expected to have the highest value when $R_f = R_g$, as mentioned in the above. In the Eulerian regime, however, the approximation of $p(\mathbf{e} | \mathbf{T})$ as a multivariate Gaussian distribution and \mathbf{T} as a Gaussian random field used for Equation (3) are not valid on the scale of R_g due to the nonlinear evolution of $\hat{\mathbf{T}}$ on the galactic scale. Thus, we consider the scales R_f much larger than R_g where these approximations still hold true. Since $\hat{\mathbf{T}}$ on two different scales of R_g and R_f are cross-correlated, it is expected that $\hat{\mathbf{e}}$ is still correlated with $\hat{\mathbf{T}}$ smoothed on the scale of $R_f \gg R_g$. The larger the difference between R_f and R_g is, the lower the value of d_t is.

2.2. Numerical Tests

Our numerical analysis is based on the data set from the Small MultiDark Planck simulation¹(SMDPL), a DM only N -body simulation conducted in a periodic box with a side length of $400 h^{-1}\text{Mpc}$ (Klypin et al. 2016) as a part of the MultiDark simulation project (Riebe et al. 2013) for a Planck universe (Planck Collaboration et al. 2014). The SMDPL tracks down the gravitational evolution of 3840^3 DM particles each of which has individual mass of $9.63 \times 10^7 h^{-1} M_{\odot}$, starting from $z = 120$ down to $z = 0$ (Klypin et al. 2016). The virialized DM halos were identified via the Rockstar halo-finding algorithm (Behroozi et al. 2013) from the spatial distributions of the DM particles at various snapshots of the SMDPL.

Through the CosmoSim database that stores all the experimental results from the MultiDark simulations, we first extract the Rockstar catalog, which provides information on a diverse set of the physical properties of the DM halos. For the current analysis, we use such information as the parent id (pId), comoving position vector (\mathbf{r}), spatial grid index, virial mass (M), coordinate vector of the largest shape ellipsoid axis (\mathbf{e}) of each Rockstar halo. The integer value of pId is used to exclude the subhalos from our analysis. For the case of a distinct halo that is not a subhalo hosted by any other larger halo, the parent id has the value of pId=-1. The coordinate vector, \mathbf{e} , is a measure of the most elongated axis of an ellipsoid to which the shape of a given Rockstar halo was fitted. From here on, the unit coordinate vector of the largest shape ellipsoid axis, $\hat{\mathbf{e}} \equiv \mathbf{e}/e$, will be called *a shape vector*.

We make a sample of the *distinct galactic halos* by selecting only those from the Rockstar catalog which meet two conditions of pId= -1 and $0.5 \leq M/(10^{11} h^{-1} M_{\odot}) < 50$. Then, we divide this sample into four subsamples which cover four different mass ranges: $0.5 \leq M/(10^{11} h^{-1} M_{\odot}) < 1$ (lowest-mass galactic halos), $1 \leq M/(10^{11} h^{-1} M_{\odot}) < 5$ (low-mass galactic halos), $5 \leq M/(10^{11} h^{-1} M_{\odot}) < 10$ (medium-mass galactic halos) and $10 \leq M/(10^{11} h^{-1} M_{\odot}) < 50$ (high-mass galactic halos), respectively. We exclude the subhalos from the analysis, since the effect of the large-scale tidal field on the subhalos are likely to be negligible compared with that of the internal nonlinear tidal fields inside the host halos. Those halos with $M < 0.5 \times 10^{11} h^{-1} M_{\odot}$ are excluded on the ground that the measurements of the shape and spin vectors of those halos are likely to be contaminated by the shot noise due to the small number of the component DM particles (Bett et al. 2007). The group and cluster size halos with $M \geq 5 \times 10^{12} h^{-1} M_{\odot}$ are also excluded since the measurements of their shapes and spins should be severely affected by their dynamical states, internal structures and recent merging events.

¹doi:10.17876/cosmosim/smdpl/

We also retrieve the cloud-in-cell density field, $\rho(\mathbf{r})$, defined on the 512^3 grids at $z = 0$ via the CosmoSim database. Then, we calculate the dimensionless density contrast field, $\delta(\mathbf{r}) = [\rho(\mathbf{r}) - \langle \rho \rangle] / \langle \rho \rangle$, where the ensemble average, $\langle \rho \rangle$, is taken over all the grids. With the help of the numerical recipe code that performs the Fast Fourier Transformation (FFT) (Press et al. 1992), we compute the Fourier amplitude of the density contrast field, $\tilde{\delta}(\mathbf{k})$, where $\mathbf{k} = k(\hat{k}_i)$ is the wave vector in the Fourier space. The inverse FFT of $\tilde{T}_{ij} = \hat{k}_i \hat{k}_j \tilde{\delta}(\mathbf{k}) \exp(-k^2 R_f^2 / 2)$ for $i, j \in \{1, 2, 3\}$ leads us to have the tidal field, $\mathbf{T}(\mathbf{r})$, smoothed on the scale of R_f .

For each subsample, we take the following steps. First, at the grid where each halo is placed, we perform a similarity transformation of $\mathbf{T}(\mathbf{r})$, to find its eigenvectors $\{\hat{\mathbf{u}}_i\}_{i=1}^3$ as well as the eigenvalues $\{\lambda_i\}_{i=1}^3$. Second, we calculate, $\{|\hat{\mathbf{u}}_i \cdot \hat{\mathbf{e}}|\}_{i=1}^3$, whose values lie in the range of $[0, 1]$. Breaking this unit interval $[0, 1]$ into seven bins with equal length of $\Delta = 1/7$, we count the number of the galactic halos, $n_{h,i}$, whose values of $|\hat{\mathbf{u}}_i \cdot \hat{\mathbf{e}}|$ fall in each bin for each $i \in \{1, 2, 3\}$. Third, the probability densities of $|\hat{\mathbf{u}}_i \cdot \hat{\mathbf{e}}|$ at each bin are determined as $p(|\hat{\mathbf{u}}_i \cdot \hat{\mathbf{e}}|) = n_{h,i} / (N_t \Delta)$ where N_t is the total number of the galactic halos contained in each subsample.

Figure 1 plots $p(|\hat{\mathbf{u}}_3 \cdot \hat{\mathbf{e}}|)$ (left panel), $p(|\hat{\mathbf{u}}_2 \cdot \hat{\mathbf{e}}|)$ (middle panels) and $p(|\hat{\mathbf{u}}_1 \cdot \hat{\mathbf{e}}|)$ (right panels) as filled circular dots for the cases of the lowest-mass (top panels), low-mass (second from the top panels), medium mass (second from the bottom panels), and high-mass (bottom panels) galactic halos. To obtain these results, we smooth $\hat{\mathbf{T}}(\mathbf{r})$ on the scale of $R_f = 5 h^{-1} \text{Mpc}$. As can be seen, for all four subsamples, the shape vector, $\hat{\mathbf{e}}$, shows a strong inclination (anti-inclination) toward the minor (major) eigenvector, $\hat{\mathbf{u}}_3$ ($\hat{\mathbf{u}}_1$), while it shows no alignment with the intermediate eigenvector, $\hat{\mathbf{u}}_2$. Note also that the higher-mass galactic halos exhibit stronger alignment (anti-alignment) tendency between $\hat{\mathbf{e}}$ and $\hat{\mathbf{u}}_3$ ($\hat{\mathbf{e}}$ and $\hat{\mathbf{u}}_1$), which are consistent with the previously reported numerical and observational results (e.g., Hahn et al. 2007b; Zhang, Yang & Faltenbacher 2009; Joachimi et al. 2013; Zhang et al. 2013; Chen et al. 2016; Hilbert et al. 2017; Xia et al. 2017; Piras et al. 2018, and references therein).

To compare the analytic model presented in Section 2.1 against these numerical results, we first calculate the mean values of $\hat{\lambda}_i$ and d_i averaged over the galactic halos contained in each subsample as

$$\langle \hat{\lambda}_i \rangle = \frac{1}{N_t} \sum_{\alpha=1}^{N_t} \hat{\lambda}_{\alpha,i} = \frac{1}{N_t} \sum_{\alpha=1}^{N_t} \left(\frac{\tilde{\lambda}_{\alpha,i}}{\sqrt{\sum_{j=1}^3 \tilde{\lambda}_{\alpha,j}^2}} \right), \quad i \in \{1, 2, 3\}, \quad (9)$$

$$\tilde{\lambda}_{\alpha,i} = \lambda_{\alpha,i} - \frac{1}{3} \sum_{j=1}^3 \lambda_{\alpha,j}, \quad i \in \{1, 2, 3\}, \quad (10)$$

$$\langle d_t \rangle = \frac{1}{N_t} \sum_{\alpha=1}^{N_t} \left[-\frac{5}{3} \sum_{i=1}^3 \hat{\lambda}_{\alpha,i} |\hat{\mathbf{u}}_{\alpha,i} \cdot \hat{\mathbf{e}}_{\alpha}|^2 \right], \quad (11)$$

where $\{\lambda_{\alpha,i}\}_{i=1}^3$ denotes a set of the three eigenvalues of \mathbf{T} at the grid where the α th DM halo of a given subsample is located, and $\hat{\mathbf{e}}_{\alpha}$ is the shape vector of the α th DM halo. Note that $\langle \hat{e}_i^2 | \hat{\mathbf{T}} \rangle$ in Equation (8) is approximated by $|\hat{\mathbf{u}}_{\alpha,i} \cdot \hat{\mathbf{e}}_{\alpha}|^2$ in Equation (11) since the measured values in numerical realizations are believed to be close to the expectation values in theory.

Substituting these mean values of $\langle \hat{\lambda}_i \rangle$ and $\langle d_t \rangle$ for $\hat{\lambda}_i$ and d_t respectively in Equations (4)-(5), we evaluate the analytical model and plot them as red solid lines in Figure 1. As can be seen, for all of the four cases of the halo mass ranges, the analytic model with the empirically determined parameter d_t describes very well not only the alignments of $\hat{\mathbf{e}}$ with $\hat{\mathbf{u}}_3$ but also simultaneously its anti-alignment with $\hat{\mathbf{u}}_1$ and no correlation with $\hat{\mathbf{u}}_2$ as well, even though no fitting process is involved. Figure 2 plots $\langle d_t \rangle$ for the four different cases of the mass ranges, showing quantitatively how the strength of the shape alignments increases with the increment of M .

Smoothing $\hat{\mathbf{T}}$ on three larger scales, $R_f = 10, 20$ and $30 h^{-1}\text{Mpc}$, we repeat the whole calculations, the results of which are shown in Figure 3 for the case of the high-mass galactic halos. The analytic model with the empirically determined parameter d_t agrees quite well with the numerical results for all of the three cases of R_f . Figure 4 shows quantitatively how the increment of R_f weakens the shape alignments. Although the alignment tendency becomes weaker as R_f increases, the shape vector, $\hat{\mathbf{e}}$, still shows significant alignment (anti-alignment) with $\hat{\mathbf{u}}_3$ ($\hat{\mathbf{u}}_1$) even for the case of $R_f = 30 h^{-1}\text{Mpc}$, which is consistent with the findings of the previous works (e.g., Xia et al. 2017).

True as it is that our analytic model shows good quantitative agreements with the numerical results for the case of the high-mass galactic halos, it is not perfect. Some discrepancies are found in the behaviors of $p(|\hat{\mathbf{u}}_3 \cdot \hat{\mathbf{e}}|)$ and $p(|\hat{\mathbf{u}}_1 \cdot \hat{\mathbf{e}}|)$ between the analytic model and the numerical results, as can be seen in the bottom panel of Figure 1. The former describes a slightly milder increase of $p(|\hat{\mathbf{u}}_3 \cdot \hat{\mathbf{e}}|)$ with $|\hat{\mathbf{u}}_3 \cdot \hat{\mathbf{e}}|$ and a slightly milder decrease of $|\hat{\mathbf{u}}_1 \cdot \hat{\mathbf{e}}|$ with $|\hat{\mathbf{u}}_1 \cdot \hat{\mathbf{e}}|$ than the latter especially for the case of the high-mass galactic halos. However, Figure 3 shows that the increment of R_f improves the agreements between the analytic model and the numerical results, which in turn implies that the discrepancies may be caused by the uncertainties associated with the approximations of $p(\mathbf{e}|\mathbf{T})$ as a multivariate Gaussian distribution and \mathbf{T} as a Gaussian random field made to derive the analytic model. The larger the scales are, the more valid these assumptions become. It explains why the analytic model works better at $R_f > 20 h^{-1}\text{Mpc}$.

2.3. Effect of the Cosmic Web

Now, we would like to investigate whether or not the strength of the alignments between the shapes of the galactic halos and the tidal eigenvectors depend on the types of the cosmic web. Following the conventional scheme (Hahn et al. 2007a), we classify the galactic halos of each subsample into the knot, filament, sheet and void halos according to the signs of the eigenvalues of \mathbf{T} at the grids where the halos are located:

$$\lambda_3 > 0 \rightarrow \text{knot}, \quad (12)$$

$$\lambda_2 > 0, \lambda_3 < 0 \rightarrow \text{filament}, \quad (13)$$

$$\lambda_1 > 0, \lambda_2 < 0 \rightarrow \text{sheet}, \quad (14)$$

$$\lambda_1 < 0 \rightarrow \text{void}. \quad (15)$$

Using only those galactic halos embedded in the same type of the cosmic web, we redo the whole analysis described in Section 2.2. Figures 5-8 show the same as Figures 1 but only with the knot, filament, sheet and void halos, respectively, showing how the shape alignment depends on the web environment. Figure 9 plots $\langle d_t \rangle$ versus M for the four different cases of the web type. As can be seen, the value of $\langle d_t \rangle$ increases more sharply with the increment of M for the cases of the sheet and void halos than for the cases of the knot and filament counterparts, which indicates that the shapes of the galactic halos in the relatively low-density regions tend to be more strongly aligned with those in the relatively high-density regions. Given that the galactic halos located in the knot and filament regions are expected to have formed earlier and undergone more severe nonlinear evolutions than those in the sheet and void regions (Gao & White 2007), the results shown in Figure 2 imply that the nonlinear evolution in denser environments will play a decisive role in diminishing the strength of the tidally induced shape alignments of the galactic halos.

It is interesting to note that the results shown in Figures 5-9 are in direct contradiction with that of Xia et al. (2017) who found the strongest shape alignments of the halos in the knot environments. We think that this apparent inconsistency between our and their results may be related the difference in the web classification scheme. In their analysis, the types of the cosmic web are classified according to the signs of the eigenvalues of the Hessian matrix of the density field. Whereas in our analysis the eigenvalues of the Hessian matrix of the gravitational potential field (i.e, tidal field) are used for the web classification.

Figures 10-13 show the same as Figures 3 but with only those high-mass galactic halos located in the knot, filament, sheet and void environments, respectively. Figure 14 plots $\langle d_t \rangle$ versus R_f for the four different cases of the web type. The decrement of the alignment strength with the increment of R_f is found for all of the four types of the cosmic web. The void

(knot) galactic halos show the most (least) rapid change of $\langle d_t \rangle$ with R_f . The web-dependence of the rate of the change of $\langle d_t \rangle$ with R_f shown in Figure 14 implies that the strength of the tidally induced shape alignments of the galactic halos is determined not only by the difference between R_g and R_f but also by the strength of the cross correlations between the tidal fields smoothed on different scales. In the denser knot and filament environments, although the nonlinearity diminishes the strength of the initially induced shape alignments with the large-scale tidal fields, the stronger cross correlations between the tidal fields smoothed on different scales slow down the rate of the decrement of the strength of the shape alignments with the increment of R_f . Whereas, in the less dense sheet and void regions where the strongest signals of the shape alignments are found on the scale of $R_f = 5 h^{-1}\text{Mpc}$, the weaker cross-correlations between the tidal fields on different scales cause the strengths of the shape alignments to decrease quite rapidly as R_f increases.

Figures 5-14 clearly demonstrate that our analytic model with the empirically determined parameter, Equations (5)-(8), makes a quantitative success in describing simultaneously and consistently the amplitudes and behaviors of the three probability density functions, $\{p(|\hat{\mathbf{u}}_i \cdot \hat{\mathbf{e}}|)\}_{i=1}^3$, for all of the cases of the galactic mass ranges M , the smoothing scales R_f and the types of the cosmic web. This notable success of our analytic model confirms the validity of the key assumption made for Equation (2) that the covariances of the shapes of the galactic halos have a linear dependence on the large-scale tidal fields (Catelan et al. 2001; Lee & Pen 2008; Hui & Zhang 2008).

3. Tidally Induced Spin Alignments

3.1. Analytic Models

Employing the analytic model based on the LTT theory developed by Lee & Pen (2000, 2001), Lee (2004) derived the probability density functions of the coordinates of the unit spin vectors, $\hat{\mathbf{s}}$, given $\hat{\mathbf{T}}$ (see also Lee et al. 2018):

$$p(|\hat{\mathbf{u}}_i \cdot \hat{\mathbf{s}}|) = \frac{1}{2\pi} \int_0^{2\pi} \left[\prod_{n=1}^3 \left(1 + c_t - 3c_t \hat{\lambda}_n^2 \right) \right]^{-\frac{1}{2}} \left(\sum_{l=1}^3 \frac{|\hat{\mathbf{u}}_l \cdot \hat{\mathbf{s}}|}{1 + c_t - 3c_t \hat{\lambda}_l^2} \right)^{-\frac{3}{2}} d\phi_{jk}, \quad (16)$$

where c_t is the spin correlation parameter in the range of $[0, 1]$ (Lee & Pen 2001). The larger value of c_t is translated into the stronger $\hat{\mathbf{u}}_2$ - $\hat{\mathbf{s}}$ alignment. Although Equation (16) is quite similar to Equation (5), there is an obvious difference: the former is expressed in terms of $\hat{\lambda}_i^2$, while the latter in terms of $\hat{\lambda}_i$. This difference originates from the fact that the covariances of the spin vectors of the galactic halos have a quadratic dependence on $\hat{\mathbf{T}}$ according to the LTT theory (Doroshkevich 1970; White 1984).

The core assumption that underlies Equation (16) is that the rescaled covariance, $\langle s_i s_j | \hat{\mathbf{T}} \rangle$, can be written as (Lee & Pen 2000)

$$\langle s_i s_j | \hat{\mathbf{T}} \rangle = \frac{1 + c_t}{3} \delta_{ij} - c_t \sum_{k=1}^3 \hat{T}_{ik} \hat{T}_{kj}. \quad (17)$$

Solving Equation (17) for c_t in the principal frame of $\hat{\mathbf{T}}$ gives ² (Lee & Pen 2001)

$$c_t = \frac{10}{3} - 10 \sum_{i=1}^3 \hat{\lambda}_i^2 \langle \hat{s}_i^2 | \hat{\mathbf{T}} \rangle. \quad (18)$$

Equation (18) enables us to evaluate the value of c_t directly from the values of $\hat{\mathbf{s}}$, $\{\hat{\lambda}_i\}_{i=1}^3$ and $\{\hat{\mathbf{u}}_i\}_{i=1}^3$. Several observational and numerical studies showed that this analytic model, Equations (16)-(18), was indeed useful and adequate in describing the tidally induced spin alignments especially in the sheet environments (e.g., Navarro et al. 2004; Trujillo et al. 2006; Lee & Erdogdu 2007; Lee et al. 2018). As mentioned in Section 1, however, the LTT theory breaks down on the mass scale below $M_t \sim 10^{12} h^{-1} M_\odot$. The numerical analyses based on recent large high-resolution N -body simulations found that the spin flip, a transition of the tendency from the $\hat{\mathbf{u}}_2$ - $\hat{\mathbf{s}}$ ($M > M_t$) alignments to the $\hat{\mathbf{u}}_3$ - $\hat{\mathbf{s}}$ alignments ($M \leq M_t$) occurs (Aragón-Calvo et al. 2007; Codis et al. 2012; Veena et al. 2018) and that the value of the transition mass scale, M_t , depends on the type of the cosmic web (Libeskind et al. 2013).

Now, we would like to construct a new model that might describe quantitatively the transition of the spin alignment tendency at M_t and its dependence on the type of the cosmic web. In the light of the previous studies which claimed that the nset of the non-Gaussianity of the tidal fields even on large scales would cause the covariance, $\langle s_i s_j | \hat{\mathbf{T}} \rangle$, to scale linearly with $\hat{\mathbf{T}}$ (Hui & Zhang 2008; Lee & Pen 2008), we first modify Equation (17) into

$$\langle s_i s_j | \hat{\mathbf{T}} \rangle = \frac{(1 + c_t + d_t)}{3} \delta_{ij} - c_t \sum_{k=1}^3 \hat{T}_{ik} \hat{T}_{kj} - d_t \hat{T}_{ij}, \quad (19)$$

where two spin correlation parameters, c_t and d_t , both lying in the range of $[0, 1]$, are introduced to correlate $\hat{\mathbf{s}}$ to $\hat{\mathbf{u}}_2$ and to $\hat{\mathbf{u}}_3$, respectively. If the first spin correlation parameter, c_t , is close to zero and the second spin correlation parameter, d_t , is close to unity, then the spin vectors $\hat{\mathbf{s}}$ will show strong alignments with $\hat{\mathbf{u}}_3$ just like the shape vectors, $\hat{\mathbf{e}}$. If c_t is close to unity and d_t is close to zero, then it will be reduced to the original model, Equation (16), which describes the $\hat{\mathbf{u}}_2$ - $\hat{\mathbf{s}}$ alignments. If both of the parameters are close to zero, then the

²In Lee et al. (2018), there was a typo in the formula. It is corrected here.

spin vectors of the galactic halos will be random having no correlations with the large-scale tidal fields.

Replacing Equation (17) by Equations (19) in the original derivation of Equation (16), it is straightforward to show that the probability density functions, $p(|\hat{\mathbf{u}}_i \cdot \hat{\mathbf{s}}|)$, can be expressed as

$$p(|\hat{\mathbf{u}}_i \cdot \hat{\mathbf{s}}|) = \frac{1}{2\pi} \int_0^{2\pi} \left[\prod_{n=1}^3 \left(1 + c_t - 3c_t \hat{\lambda}_n^2 + d_t - 3d_t \hat{\lambda}_n \right) \right]^{-\frac{1}{2}} \times \left[\sum_{l=1}^3 \left(\frac{|\hat{\mathbf{u}}_l \cdot \mathbf{s}|}{1 + c_t - 3c_t \hat{\lambda}_l^2 + d_t - 3d_t \hat{\lambda}_l} \right) \right]^{-\frac{3}{2}} d\phi_{jk}. \quad (20)$$

Equation (18), which was originally derived in the LTT theory, holds true even when the covariance, $\langle \hat{s}_i \hat{s}_j | \hat{\mathbf{T}} \rangle$, has an additional term, since the second and third terms in Equation (19) are uncorrelated due to $\langle \hat{T}_{ik} \hat{T}_{kl} \hat{T}_{lj} \rangle = 0$ (see Appendix E in Lee & Pen 2001). Thus, the same formula as Equation (18) can be used to obtain the value of c_t for this new model. Likewise, the same formula as Equation (8) but with $\hat{\mathbf{e}}$ replaced by $\hat{\mathbf{s}}$ can be used to obtain the value d_t as

$$d_t = -\frac{5}{3} \sum_{i=1}^3 \hat{\lambda}_i \langle \hat{s}_i^2 | \hat{\mathbf{T}} \rangle. \quad (21)$$

In Section 3.2, we will numerically test three models for the galaxy spin alignments, **model I**, **model II** and **model III**. The **model III** is Equation (20) with two non-zero parameters, c_t and d_t . The **model I** is Equation (20) with $d_t = 0$. It is identical to the original model based on the LTT theory, Equation (16). The **model II** is Equation (20) with $c_t = 0$. It has the same functional form as Equation (5) for the tidally induced shape alignments.

3.2. Numerical Tests

To numerically obtain three probability density functions, $\{p(|\hat{\mathbf{u}}_i \cdot \hat{\mathbf{s}}|)\}_{i=1}^3$, we perform the exactly same calculations as presented in Section 2.2, but with $\hat{\mathbf{e}}$ replaced by $\hat{\mathbf{s}}$. For the evaluation of the three analytic models, we first determine the ensemble values of $\langle c_t \rangle$ and $\langle d_t \rangle$ for each subsample as,

$$\langle c_t \rangle = \frac{1}{N_t} \sum_{\alpha=1}^{N_t} \left[\frac{10}{3} - 10 \sum_{i=1}^3 \hat{\lambda}_{\alpha,i}^2 |\hat{\mathbf{u}}_{\alpha,i} \cdot \hat{\mathbf{s}}_{\alpha}|^2 \right], \quad (22)$$

$$\langle d_t \rangle = \frac{1}{N_t} \sum_{\alpha=1}^{N_t} \left[-\frac{5}{3} \sum_{i=1}^3 \hat{\lambda}_{\alpha,i} |\hat{\mathbf{u}}_{\alpha,i} \cdot \hat{\mathbf{s}}_{\alpha}|^2 \right], \quad (23)$$

and put these ensemble average values into Equation (20) to evaluate the **model III**. Putting $\langle c_t \rangle$ ($\langle d_t \rangle$) into Equation (20) and setting $\langle d_t \rangle$ ($\langle c_t \rangle$) at zero, we evaluate the **mode I** (**model II**).

Figure 15 plots the numerically obtained probability density functions, $\{p(|\hat{\mathbf{u}}_i \cdot \hat{\mathbf{s}}|)\}_{i=1}^3$ (filled dots), and compares them with the **model I** (blue lines), **model II** (green lines) and **model III** (red lines). As can be seen, the three functions, $\{p(|\hat{\mathbf{u}}_i \cdot \hat{\mathbf{s}}|)\}_{i=1}^3$, have much lower amplitudes than $\{p(|\hat{\mathbf{u}}_i \cdot \hat{\mathbf{e}}|)\}_{i=1}^3$ displayed in Figure 1. It indicates that the spin vectors of the galactic halos are much less strongly aligned with the large-scale tidal fields than the shape vectors, which is consistent with the results of the previous numerical and observational studies (e.g., Hahn et al. 2007b; Forero-Romero et al. 2014; Zhang et al. 2015).

The occurrence of the spin-flip phenomenon is indeed witnessed: For the case of the lower mass galactic halos with $M < 10^{12} h^{-1} M_{\odot}$, the unit spin vectors, $\hat{\mathbf{s}}$, tend to be aligned not with the intermediate eigenvectors, $\hat{\mathbf{u}}_2$, but with the minor eigenvectors, $\hat{\mathbf{u}}_3$, while the high-mass galactic halos with $M \geq 10^{12} h^{-1} M_{\odot}$, exhibit the stronger alignments of $\hat{\mathbf{s}}$ with $\hat{\mathbf{u}}_2$ rather than with $\hat{\mathbf{u}}_3$, which is quite consistent with the previous numerical results (e.g., Aragón-Calvo et al. 2007; Hahn et al. 2007b; Codis et al. 2012; Libeskind et al. 2013; Dubois et al. 2014; Chen et al. 2016; Veena et al. 2018).

The strength of the $\hat{\mathbf{u}}_3$ - $\hat{\mathbf{s}}$ alignments tends to decrease with M , while the strengths of the $\hat{\mathbf{u}}_2$ - $\hat{\mathbf{s}}$ alignments increases with M . These opposite trends can be quantitatively described by the variation of the first and second spin correlation parameters with M as shown in the top and bottom panels of Figure 16, respectively. As can be seen, $\langle d_t \rangle$ is larger than $\langle c_t \rangle$ in the lower mass range of $M < 10^{12} h^{-1} M_{\odot}$ but drops below $\langle c_t \rangle$ in the higher mass range of $M \geq 10^{12} h^{-1} M_{\odot}$. The transition mass scale of the spin-flip corresponds to the moment when $\langle d_t \rangle$ becomes lower than $\langle c_t \rangle$.

For the case of the lowest and low-mass galactic halos with $M < 5 \times 10^{11} h^{-1} M_{\odot}$, both of the models II and III succeed in matching simultaneously the amplitudes and behaviors of the three numerically obtained probability density functions. The **model II** is almost identical to the **model III** in these low-mass ranges, since the values of $\langle c_t \rangle$ obtained via Equation (22) are low for these cases. It is also worth noting that the signal of the strong $\hat{\mathbf{u}}_1$ - $\hat{\mathbf{s}}$ anti-alignments is found to increase with M whose behavior is well described by both of the model II and III. The success of the **model II** and **model III** and the failure of the **model I** in describing the amplitudes and behaviors of $p(|\hat{\mathbf{u}}_3 \cdot \hat{\mathbf{s}}|)$ and $p(|\hat{\mathbf{u}}_1 \cdot \hat{\mathbf{s}}|)$ are also found for the case of the medium-mass halos (second from the bottom panels in Figure 15).

It is, however, interesting to note that in this medium-mass range the spin vectors, $\hat{\mathbf{s}}$, exhibit a weak but non-negligible alignment with the intermediate eigenvectors, $\hat{\mathbf{u}}_2$, which tendency is properly described by both of `model I` and `model III` but not by the `model II`. For the case of the high-mass galactic halos, the unit spin vectors, $\hat{\mathbf{s}}$, turn out to be more strongly aligned with $\hat{\mathbf{u}}_2$ than with $\hat{\mathbf{u}}_3$, which cannot be described by the `model II`. But, the alignments of $\hat{\mathbf{s}}$ with $\hat{\mathbf{u}}_3$ and its anti-alignments with $\hat{\mathbf{u}}_1$ are still well described by the `model II` and `model III` but not by the `model I`. Thus, it is only the `model III` that agrees concurrently and consistently with the numerically obtained three probability density functions, $p(|\hat{\mathbf{u}}_3 \cdot \hat{\mathbf{s}}|)$, $p(|\hat{\mathbf{u}}_2 \cdot \hat{\mathbf{s}}|)$, and $p(|\hat{\mathbf{u}}_1 \cdot \hat{\mathbf{s}}|)$, in all of the four mass ranges.

Figure 17 shows the same as the bottom panels of Figure 15 but for the cases that the tidal fields are smoothed on three larger scales of $R_f = 10, 20$ and $30 h^{-1}\text{Mpc}$, in the top, middle and bottom panels, respectively. As can be seen, the increment of R_f decreases the alignment strengths even more rapidly than for the case of the shape alignments. Note that it is only the `model III` that succeeds in making good simultaneous descriptions of the amplitudes and behaviors of $\{p(|\hat{\mathbf{u}}_i \cdot \hat{\mathbf{s}}|)\}_{i=1}^3$ for all of the three cases of R_f .

Although the `model III` achieves overall good agreements with the numerical results, some discrepancies between its description and the numerical results are found. As can be seen in Figures 15-17, the numerically obtained three probability functions display substantially fluctuating behaviors especially for the case of the high-mass galactic halos. However, the increment of R_f reduces these discrepancies as shown in Figure 17, which implies that the inaccuracies associated with the approximations of \mathbf{T} as a Gaussian random field and $p(\mathbf{s}|\mathbf{T})$ as a multivariate Gaussian distribution in the derivation of Equation (20) should be largely responsible for these discrepancies.

The uncertainties involved in the measurements of the spin vectors of the galactic halos may be another source of the discrepancies. Since the spin direction of a galactic halo is dominantly determined by the positions and velocities of the outmost DM particles from the halo center, its measurement would depend sensitively on the dynamical state of the galactic halo, halo-finding algorithm and definition of the virial radius. If a high-mass galactic halo has yet to be fully relaxed and/or in the middle of merging, containing multiple substructures, the measurement of its spin direction is likely to suffer from substantial uncertainties, which in turn would cause mismatches between the analytical and the numerical results on the spin alignments with the large-scale tidal field.

Figure 18 shows how the first and second spin parameters vary with R_f for the high-mass galactic halos in the top and bottom panels, respectively. As can be seen, both of the parameters decrease with the increment of R_f . The two parameters, however, show different variations with M . The first spin parameter, $\langle c_i \rangle$, decreases more rapidly with

the increment of R_f than the second spin parameter, $\langle d_t \rangle$. It is found that $\langle c_t \rangle > \langle d_t \rangle$ at $R_f \leq 20 h^{-1}\text{Mpc}$, while $c_t < d_t$ at $R_f = 30 h^{-1}\text{Mpc}$. This result implies that the occurrence of the spin flip phenomenon is contingent on the sizes of the large-scale structures. Suppose that the galaxies with masses in the range of $0.5 \leq M/(10^{11} h^{-1} M_\odot) \leq 50$ embedded in a coherent large-scale structure like a filament with size $R_f \geq 30 h^{-1}\text{Mpc}$. According to our results, the spin vectors of those galaxies would not flip, with their spins always aligned with the elongated axes of the host filament since $\langle d_t \rangle$ is always higher than $\langle c_t \rangle$ in the given mass range (see Section 3.3).

3.3. Effect of the Cosmic Web

Following the same procedure as presented in Section 2.3, we investigate how the probability density functions, $\{p(|\hat{\mathbf{u}}_i \cdot \hat{\mathbf{s}}|)\}_{i=1}^3$, depend on the type of the cosmic web. Figures 19-22 show the same as Figure 15 but only with the galactic halos located in the knot, filament, sheet and void environments, respectively. In the knot environments (Figure 19), the unit spin vectors, $\hat{\mathbf{s}}$, of the galactic halos are found strongly aligned with the minor eigenvector $\hat{\mathbf{u}}_3$ in all of the four mass ranges (i.e., no spin-flip). For the cases of the lowest-mass, low-mass and medium-mass knot galactic halos, we find $\hat{\mathbf{s}}$ to be slightly anti-aligned rather than aligned with $\hat{\mathbf{u}}_2$, while the high-mass knot galactic halos show weak $\hat{\mathbf{u}}_2$ - $\hat{\mathbf{s}}$ alignments. Both of the `model II` and `model III` describe well the $\hat{\mathbf{u}}_3$ - $\hat{\mathbf{s}}$ alignment and the $\hat{\mathbf{u}}_1$ - $\hat{\mathbf{s}}$ anti-alignment. However, `model II` cannot describe the observed tendency of the $\hat{\mathbf{u}}_2$ - $\hat{\mathbf{s}}$ anti-alignment in the mass scale of $5 \leq M/(10^{11} h^{-1} M_\odot) < 10$ while the `model III` can. It is interesting to see that the `model I` describes better the observed $\hat{\mathbf{u}}_2$ - $\hat{\mathbf{s}}$ anti-alignments in the medium-mass range better than the `model II` although it still notoriously fails in describing the observed strong $\hat{\mathbf{u}}_3$ - $\hat{\mathbf{s}}$ alignments and $\hat{\mathbf{u}}_1$ - $\hat{\mathbf{s}}$ anti-alignments.

The filament galactic halos yield much stronger $\hat{\mathbf{u}}_3$ - $\hat{\mathbf{s}}$ alignment and $\hat{\mathbf{u}}_1$ - $\hat{\mathbf{s}}$ anti-alignment in all of the four mass ranges than the knot counterpart, although the behaviors of $\{p(|\hat{\mathbf{u}}_i \cdot \hat{\mathbf{s}}|)\}_{i=1}^3$ between the two cases are quite similar to each other (Figure 20). The high-mass filament galactic halos show a substantial $\hat{\mathbf{u}}_2$ - $\hat{\mathbf{s}}$ alignment whose strength is comparable to that of the $\hat{\mathbf{u}}_3$ - $\hat{\mathbf{s}}$ (i.e., the occurrence of the spin flip). Although the `model III` works quite well in matching the numerically obtained probability density functions, it is interesting to note that the `model II` gives a better description of $p(|\hat{\mathbf{u}}_2 \cdot \hat{\mathbf{s}}|)$ than the `model III` in the mass range of $M < 10^{12} h^{-1} M_\odot$.

The sheet galactic halos exhibit a different trend (Figure 21). Their spin vectors tend to lie in the plane spanned by $\hat{\mathbf{u}}_2$ and $\hat{\mathbf{u}}_3$, being orthogonal to $\hat{\mathbf{u}}_1$. The increment of M leads to the stronger $\hat{\mathbf{u}}_2$ - $\hat{\mathbf{s}}$ alignment and $\hat{\mathbf{u}}_1$ - $\hat{\mathbf{s}}$ anti-alignment but weaker $\hat{\mathbf{u}}_3$ - $\hat{\mathbf{s}}$ alignment. For the

case of the lowest-mass and low-mass sheet galactic halos, the $\hat{\mathbf{u}}_2$ - $\hat{\mathbf{s}}$ alignment tendency is weaker than the $\hat{\mathbf{u}}_3$ - $\hat{\mathbf{s}}$ alignment. For the case of the medium-mass sheet galactic halos, the $\hat{\mathbf{u}}_2$ - $\hat{\mathbf{s}}$ alignment begins to exceed in strength the $\hat{\mathbf{u}}_3$ - $\hat{\mathbf{s}}$ alignment (i.e., occurrence of the spin flip). The strongest signal of the $\hat{\mathbf{u}}_2$ - $\hat{\mathbf{s}}$ alignments is found from the high-mass sheet galactic halos, which result is consistent with the previous numerical finding of Hahn et al. (2007a). As can be seen, only the `Model III` succeeds in describing simultaneously and consistently the behaviors of $\{p(|\hat{\mathbf{u}}_i \cdot \hat{\mathbf{s}}|)\}_{i=1}^3$, fairly well for the case of the sheet galactic halos in all of the four mass ranges.

This result is inconsistent with the observational finding of Zhang et al. (2015) that the galaxies in the knot environments exhibited the strongest spin alignments with the tidal fields. We suspect that two factors may have caused this inconsistency between the numerical and observational results on the web dependence of the spin alignments. First, the difference in the way in which the tidal fields were constructed. In the work of Zhang et al. (2015), the tidal fields, $\hat{\mathbf{T}}$, were constructed from the spatial distributions of the galaxy groups, while in the SMDPL the spatial distribution of the DM particles were used. Second, the difference in the measurements of $\hat{\mathbf{s}}$: In the observational analysis of Zhang et al. (2015), the unit spin vectors $\hat{\mathbf{s}}$ were determined from the luminous parts of the galaxies while in the current numerical analyses, all of the constituent DM particles determine $\hat{\mathbf{s}}$.

The weakest spin alignments with the large-scale tidal fields are found in the void environments (Figure 22). Although the signals are quite lower than those yielded by the sheet galactic halos, the behaviors of $\{p(|\hat{\mathbf{u}}_i \cdot \hat{\mathbf{s}}|)\}_{i=1}^3$ obtained from the void galactic halos are quite similar to those from the sheet galactic halos: the alignments of $\hat{\mathbf{s}}$ with $\hat{\mathbf{u}}_2$ and $\hat{\mathbf{u}}_3$. The former (the latter) alignment become stronger (weaker) with the increment of M . For the lowest-mass and low-mass void galactic halos (top two panels), the $\hat{\mathbf{u}}_3$ - $\hat{\mathbf{s}}$ alignment is slightly stronger than the $\hat{\mathbf{u}}_2$ - $\hat{\mathbf{s}}$ alignment. Only the `Model III` pulls it off to describe simultaneously the behaviors of $\{p(|\hat{\mathbf{u}}_i \cdot \hat{\mathbf{s}}|)\}_{i=1}^3$. For the case of the medium-mass and high-mass void galactic halos, however, the large errors make it difficult to interpret the numerical results and to make a fair comparison of them with the three models.

Figures 23 and 24 plot $\langle c_t \rangle$ and $\langle d_t \rangle$ versus M for the four different web types, respectively. Although the increment of the first spin correlation parameter, $\langle c_t \rangle$, with M is universally shown, the increment rate sensitively depends on the web type. The most (least) rapid change of $\langle c_t \rangle$ with M is found from the sheet (knot) galactic halos. Meanwhile, the second spin correlation parameter, $\langle d_t \rangle$, does not show strong variations with M . For the case of the high-mass filament and void galactic halos, however, it shows an abrupt decrement with M .

Defining the transition mass, M_t , as the one beyond which $\langle c_t \rangle$ exceeds $\langle d_t \rangle$, we expect

the galactic halos with $M > M_t$ ($M \leq M_t$) to exhibit the preferential $\hat{\mathbf{u}}_2\text{-}\hat{\mathbf{s}}$ ($\hat{\mathbf{u}}_3\text{-}\hat{\mathbf{s}}$) alignment. The results shown in Figures 23 and 24 imply that the value of M_t depends on the web type, as shown in Libeskind et al. (2013). For the case of the knot galactic halos, no spin flip occurs in the given whole mass range since $\langle d_t \rangle$ is always larger than $\langle c_t \rangle$. The spin flip of the filament (sheet) galactic halos is expected to occur around $M_t \sim 5 \times 10^{12} h^{-1} M_\odot$ ($M_t \sim 10^{12} h^{-1} M_\odot$), while the void galactic halos show the lowest transition mass scale, $M_t \sim 5 \times 10^{11} h^{-1} M_\odot$.

As done in Section 2.3, smoothing the tidal fields on three larger scales R_f and repeating the whole calculation for each case of R_f , we investigate the dependence of the tendency and strength of the spin alignments on R_f for the case of the high-mass galactic halos. Figures 25-28 plot the same as the bottom panels of Figures 19-22, respectively, but for the cases of $R_f = 10, 20, 30 h^{-1}\text{Mpc}$. As can be seen, whatever type of the cosmic web the galactic halos are embedded in, the increment of R_f always decreases the alignment strength, which is well described by the `model III`.

For the cases of the high-mass galactic halos in the knot and filament regions, the increment of R_f just decreases the strength of the spin alignments but does not change its tendency (Figures 25-26). However, for the case of the high-mass sheet galactic halos (Figure 27), it changes both of the strength and the tendency of the spin alignments. On the scales of $R_f = 10$ and $20 h^{-1}\text{Mpc}$, the high-mass sheet galactic halos show the stronger $\hat{\mathbf{u}}_2\text{-}\hat{\mathbf{s}}$ alignments than the $\hat{\mathbf{u}}_3\text{-}\hat{\mathbf{s}}$ alignments. But, on the larger scale of $R_f = 30 h^{-1}\text{Mpc}$, we witness a different tendency, the $\hat{\mathbf{u}}_3\text{-}\hat{\mathbf{s}}$ alignments seem slightly stronger than the $\hat{\mathbf{u}}_2\text{-}\hat{\mathbf{s}}$ alignments. In other words, if the sheet environment is defined on the scale equal to or larger than $30 h^{-1}\text{Mpc}$, no spin-flip will occur in the given mass range. Since both of $\hat{\mathbf{u}}_2$ and $\hat{\mathbf{u}}_3$ span the plane of a sheet (Zel'dovich 1970), our result shown in Figure 27 supports the claim of Hahn et al. (2007b) that the spin vectors of the DM halos have a universal tendency of lying in the plane of the sheet, regardless of the halo mass.

4. Summary and Discussion

To study the large-scale tidal effect on the spin and shape orientations of the galaxies and the spin-flip phenomenon, we have considered three different analytic models, the `model I`, `model II` and `model III`. The `model I`, Equation (16), which was originally developed by Lee & Pen (2000) based on the LTT theory, describes the alignment tendency between the galaxy spin vectors, $\hat{\mathbf{s}}$, and the intermediate eigenvectors, $\hat{\mathbf{u}}_2$, of the large-scale tidal field, \mathbf{T} . The `model II`, Equation (5), has been constructed here to describe the alignments (anti-alignments) of the galaxy shapes, $\hat{\mathbf{e}}$, with the minor (major) eigenvectors, $\hat{\mathbf{u}}_3$ ($\hat{\mathbf{u}}_1$) of \mathbf{T} .

This model is based on the first order Lagrangian perturbation theory according to which the major principal axes of the inertia momentum tensors of the galactic halos are perfectly aligned with the minor principal axes of the local tidal tensors in the Lagrangian regime. The `model III`, Equation (20), is a practical formula constructed by combining the `model I` and `model II` to describe simultaneously the tidally induced shape and spin alignments.

The `model I` (`model II`) carries a single parameter, c_t (d_t), which measures the strength of the alignment with $\hat{\mathbf{u}}_2$ ($\hat{\mathbf{u}}_3$). The `model III` carries two parameters, c_t and d_t , whose relative ratio determines the transition mass scale for the occurrence of the spin-flip. The first parameter, c_t , would reach the maximum value of unity, if the inertia momentum tensors of the galaxies are uncorrelated with the surrounding tidal tensors, while the second parameter, d_t , will attain the value of unity if the two tensors are perfectly correlated. These parameters can be empirically determined by Equation (22) directly from the measured values of $\hat{\mathbf{e}}$ and $\hat{\mathbf{s}}$ in the principal frame of $\hat{\mathbf{T}}$ without resorting to any fitting procedure.

To numerically test the three analytic models, we have utilized the density fields and the Rockstar halo catalogs extracted from the SMDPL simulations (Klypin et al. 2016). Constructing the unit traceless tidal tensor, $\hat{\mathbf{T}}$, smoothed on the scale of $R_f = 5 h^{-1} \text{Mpc}$ from the density fields given on the 512^3 grids that constitute the simulation box of volume $400^3 h^{-3} \text{Mpc}^3$ and selecting the galactic halos in the mass range of $0.5 \leq M/(10^{11} h^{-1} M_\odot) \leq 50$ from the Rockstar catalog, we have first numerically obtained the probability density functions of the tidally induced shape alignments, $\{p(|\hat{\mathbf{u}}_i \cdot \hat{\mathbf{e}}|)\}_{i=1}^3$ (see Figures 1-3). The numerical results have clearly shown that $\hat{\mathbf{e}}$ has a tendency to be strongly aligned (anti-aligned) with $\hat{\mathbf{u}}_3$ ($\hat{\mathbf{u}}_1$) but no correlation with $\hat{\mathbf{u}}_2$. Investigating the dependence of the strength of the tidally induced shape alignments on M , R_f , and the type of the cosmic web, it has been found that the more massive galactic halos yield stronger $\hat{\mathbf{u}}_3$ - $\hat{\mathbf{e}}$ alignments ($\hat{\mathbf{u}}_1$ - $\hat{\mathbf{e}}$ anti-alignments) and that the increment of R_f weakens the alignment tendency (see Figures 4). These numerical results are consistent with what the previous works already found (Joachimi et al. 2013; Zhang et al. 2013; Chen et al. 2016; Hilbert et al. 2017; Xia et al. 2017; Piras et al. 2018).

The strongest (weakest) $\hat{\mathbf{u}}_3$ - $\hat{\mathbf{e}}$ alignments are found from the void (knot) galactic halos (see Figures 5-8), which seem inconsistent with the previous numerical result that the DM halos showed the strongest shape alignments in the knot environments (Xia et al. 2017). This inconsistency has been ascribed to the different classification schemes used in the two analyses. The sheet galactic halos yield much stronger shape alignment tendency than the knot and filament galactic halos in the whole mass range, which result is consistent with what Hahn et al. (2007a) found. In the lowest and low mass range ($0.5 \leq M/[10^{11} h^{-1} M_\odot] < 5$), the knot and filament galactic halos show similar strengths of the shape alignments. In the medium-mass ($5 \leq M/[10^{11} h^{-1} M_\odot] < 10$) and high-mass ($10 \leq M/[10^{11} h^{-1} M_\odot] < 50$)

ranges, the shape alignments of the filament galactic halos become stronger than the knot counterparts (Figure 9). These numerical results imply that the void and sheet galactic halos retain best the tidally induced shape alignments, while the evolution of the galactic halos in the dense environments like the knots and filaments has an effect of deviating the directions of their shapes from the tidally induced inclinations.

The comparison with the numerical results revealed the success of the `model II` in describing the amplitudes and behaviors of $\{p(|\hat{\mathbf{u}}_i \cdot \hat{\mathbf{e}}|)\}_{i=1}^3$, for all of the cases of M , R_f and the type of the cosmic web. For the shape alignments, the `model III` turns out to be identical to the `model II`. For all of the four cases of the web type, the increment of R_f has been found to decrease the strength of the tidally induced shape alignments but improve the agreements between the `model III` and the numerical results (Figure 10-14). We interpret this result as an evidence supporting the scenario that the nonlinear evolution has an effect of diminishing the strength of the tidally induced shape alignments.

In a similar manner, we have numerically determined the probability density functions of the tidally induced spin alignments, $\{p(|\hat{\mathbf{u}}_i \cdot \hat{\mathbf{s}}|)\}_{i=1}^3$, explored their dependences on M , R_f and the web type, and compared the results with the three analytic models. The tidally induced spin alignments have been found significant but quite weak compared with the shape alignments (Figures 15-16), consistent with the results from the previous works (e.g., Hahn et al. 2007b; Forero-Romero et al. 2014; Zhang et al. 2015). The occurrence of the spin-flip phenomenon has been witnessed. For the case of $R_f = 5 h^{-1}\text{Mpc}$, the lowest-mass, low-mass and medium-mass galactic halos show strong $\hat{\mathbf{u}}_3\text{-}\hat{\mathbf{s}}$ alignments and negligible $\hat{\mathbf{u}}_2\text{-}\hat{\mathbf{s}}$ alignments, while the high-mass galactic halos exhibit strong $\hat{\mathbf{u}}_2\text{-}\hat{\mathbf{s}}$ alignments, which results have confirmed the claims of the previous works (Aragón-Calvo et al. 2007; Paz et al. 2008; Zhang, Yang & Faltenbacher 2009; Codis et al. 2012; Libeskind et al. 2013; Trowland et al. 2013; Dubois et al. 2014; Chen et al. 2016; Veena et al. 2018).

However, we have noted that the spin-flip does not occur abruptly at a certain fixed transition mass scale. Rather it is a gradual transition of the spin alignment tendency that proceeds over a broader mass range, depending on R_f (Figures 17-18). For the case of $R_f = 5 h^{-1}\text{Mpc}$, the high-mass galactic halos have been found to yield stronger $\hat{\mathbf{u}}_2\text{-}\hat{\mathbf{s}}$ and weaker but significant $\hat{\mathbf{u}}_3\text{-}\hat{\mathbf{s}}$ alignments, while the medium-mass galactic halos exhibit strong $\hat{\mathbf{u}}_3\text{-}\hat{\mathbf{s}}$ and much weaker $\hat{\mathbf{u}}_2\text{-}\hat{\mathbf{s}}$ alignments. For the case of $R_f \geq 10 h^{-1}\text{Mpc}$, however, the high-mass galactic halos exhibit stronger $\hat{\mathbf{u}}_3\text{-}\hat{\mathbf{s}}$ and weaker but significant $\hat{\mathbf{u}}_2\text{-}\hat{\mathbf{s}}$ alignments.

The strengths of the tidally induced spin alignments have been also found to sensitively vary with the types of the cosmic web (see Figures 19-28), which supports the claim of Libeskind et al. (2013). The strongest (weakest) signals of the tidally induced spin alignments have been found from the sheet (void) galactic halos, while the filament galactic halos

have been found to have stronger spin alignments than the knot counterparts in the whole mass range (Figures 23-24). These results are inconsistent with the observational finding of Zhang et al. (2015) that the knot galaxies exhibited the strongest signals of the spin alignments. We have suspected that this inconsistency might be related to the construction of the tidal field from the galaxy groups and the determination of the spin axes of the galaxies from their stellar components in the observational analysis.

Determining empirically $\langle c_t \rangle$ and $\langle d_t \rangle$ from the numerical data (Figures 23-24) and defining the condition for the occurrence of the spin flip as $\langle c_t \rangle > \langle d_t \rangle$, we have quantitatively investigated how the occurrence and the transition mass scale, M_t , of the spin-flip phenomenon depend on the size and type of the cosmic web and found the following:

1. Regardless of the web type, the transition mass scale, M_t , of the spin-flip increases with the increment of R_f .
2. The knot galactic halos do not show any spin-flip phenomenon. That is, the unit spin vectors, $\hat{\mathbf{s}}$, of the knot galactic halos are always preferentially aligned with $\hat{\mathbf{u}}_3$ rather than with $\hat{\mathbf{u}}_2$ in the whole mass range, regardless of the value of R_f (Figure 25).
3. For the case of the filament galactic halos, the spin flip occurs around $M_t \sim 5 \times 10^{12} h^{-1} M_\odot$ when $R_f = 5 h^{-1} \text{Mpc}$. At the larger scale of $R_f > 5 h^{-1} \text{Mpc}$, the value of M_t exceeds the galactic mass scales, i.e, $M_t > 5 \times 10^{12} h^{-1} M_\odot$ (Figure 26).
4. In the sheet environment, the transition mass scale has a lower value than in the filaments: $M_t \sim 10^{12} h^{-1} M_\odot$ when $R_f = 5 h^{-1} \text{Mpc}$. Only when R_f reaches $30 h^{-1} \text{Mpc}$, the value of M_t becomes larger than the galactic mass scale (Figure 27).
5. The void galactic halos yield the lowest transition mass scale, $M_t \sim 5 \times 10^{11} h^{-1} M_\odot$ when $R_f = 5 h^{-1} \text{Mpc}$. At the larger scales, the number of the void galactic halos is too low to produce any significant signals (Figure 28).

It is interesting to note that our results on the web and mass dependence of the spin-flip phenomenon are consistent with the theoretical explanation of Codis et al. (2015), according to which the misalignments between the inertia momentum and tidal tensors in the anisotropic environments like the filaments and sheets are largely responsible for the occurrence of the spin flip. In line with their theoretical explanation, we interpret no occurrence of the spin flip in the knot environments as an evidence for the stronger alignments between the two tensors in the dense environments. In other words, in the knot regions where the tidal tensors are more isotropic, the inertia momentum and tidal tensors may be more strongly

aligned with each other, which plays a role in suppressing the occurrence of the spin-flip of the knot galaxies.

It has also been clearly demonstrated in the current work that the `model III` succeeds in describing consistently and simultaneously the numerical results of the tidally induced shape and spin alignments for all of the cases of M , R_f and type of the cosmic web, while the `model I` and `model II` fail. Showing that the `model III` works better as R_f increases, we have ascribed the slight mismatches between the numerical results and the `model III` to the inaccuracies caused by the approximations of $p(\mathbf{s}|\mathbf{T})$ as a multivariate Gaussian distribution and $\hat{\mathbf{T}}$ as a Gaussian random field made in the construction of the `model III`. We also suspect that the uncertainties in the measurements of $\hat{\mathbf{s}}$ and $\hat{\mathbf{e}}$ caused by the simple assumptions of each galactic halo having a perfect ellipsoidal shape and no substructure in a completely relaxed dynamical state must contribute to the mismatches.

We conclude that the `model III` is an effective practical model for the spin and the shape alignments of the galactic halos with the large-scale tidal fields, providing an analytic tool with which the condition of the spin flip occurrence as well as its dependence on the properties of the large-scale structures can be quantitatively described. Its good accord with the numerical results supports the scenario that the occurrence of the spin flip phenomenon is associated more with the geometrical properties of the large-scale tidal field as well as the interactions of the galactic halos with the cosmic web rather than with the physical processes during the nonlinear evolution (see Libeskind et al. 2013; Codis et al. 2015; Wang & Kang 2017; Veena et al. 2018).

Given that the `model III` is expressed in terms of the linear quantities, it may provide another independent probe of the background cosmology. For this purpose, however, a couple of back-up works will have to be done. First, as suspected in our analysis, differences in the schemes used to to construct the tidal fields, to measure the shape and spin axes of the galaxies, and to classify the cosmic web would yield different patterns in the dependence of the tidally induced shape and spin alignments on the sizes and types of the cosmic web. Thus, it will be necessary to test the robustness of the `model III` against the variations of the schemes. Second, it will be also essential to examine its validity using the numerical results for alternative cosmologies such as models with modified gravity, coupled dark energy, massive neutrinos, primordial non-Gaussianity, anisotropic inflation and so forth. Our future work is in this direction.

The CosmoSim database used in this paper is a service by the Leibniz-Institute for Astrophysics Potsdam (AIP). The MultiDark database was developed in cooperation with the Spanish MultiDark Consolider Project CSD2009-00064. I gratefully acknowledge the Gauss

Centre for Supercomputing e.V. (www.gauss-centre.eu) and the Partnership for Advanced Supercomputing in Europe (PRACE, www.prace-ri.eu) for funding the MultiDark simulation project by providing computing time on the GCS Supercomputer SuperMUC at Leibniz Supercomputing Centre (LRZ, www.lrz.de). The Bolshoi simulations have been performed within the Bolshoi project of the University of California High-Performance AstroComputing Center (UC-HiPACC) and were run at the NASA Ames Research Center.

I thank an anonymous referee for providing very helpful suggestions and constructive criticisms. I acknowledge the support of the Basic Science Research Program through the National Research Foundation (NRF) of Korea funded by the Ministry of Education (NO. 2016R1D1A1A09918491). I was also partially supported by a research grant from the NRF of Korea to the Center for Galaxy Evolution Research (No.2017R1A5A1070354).

REFERENCES

- Altay, G., Colberg, J. M., & Croft, R. A. C. 2006, MNRAS, 370, 1422
- Aragón-Calvo, M. A., van de Weygaert, R., Jones, B. J. T., & van der Hulst, J. M. 2007, ApJ, 655, L5
- Bailin, J., & Steinmetz, M. 2005, ApJ, 627, 647
- Bett, P., Eke, V., Frenk, C. S., et al. 2007, MNRAS, 376, 215
- Bett, P. E., & Frenk, C. S. 2012, MNRAS, 420, 3324
- Bett, P. E., & Frenk, C. S. 2016, MNRAS, 461, 1338
- Behroozi, P. S., Wechsler, R. H., & Wu, H.-Y. 2013, ApJ, 762, 109
- Blazek, J., McQuinn, M., & Seljak, U. 2011, JCAP, 5, 010
- Blazek, J., Vlah, Z., & Seljak, U. 2015, JCAP, 8, 015
- Brinckmann, T., Lindholmer, M., Hansen, S., & Falco, M. 2016, JCAP, 4, 007
- Buchert, T. 1992, MNRAS, 254, 729
- Catelan, P., Kamionkowski, M., & Blandford, R. D. 2001, MNRAS, 320, L7
- Chen, S., Wang, H., Mo, H. J., & Shi, J. 2016, ApJ, 825, 49
- Chen, Y.-C., Ho, S., Blazek, J., et al. 2018, arXiv:1805.00159
- Codis, S., Pichon, C., Devriendt, J., et al. 2012, MNRAS, 427, 3320
- Codis, S., Pichon, C., & Pogosyan, D. 2015, MNRAS, 452, 3369
- Crittenden, R. G., Natarajan, P., Pen, U.-L., & Theuns, T. 2001, ApJ, 559, 552
- Doroshkevich, A. G. 1970, Astrofizika, 6, 581
- Dubois, Y., Pichon, C., Welker, C., et al. 2014, MNRAS, 444, 1453
- Forero-Romero, J. E., Contreras, S., & Padilla, N. 2014, MNRAS, 443, 1090
- Gao, L., & White, S. D. M. 2007, MNRAS, 377, L5
- Hahn, O., Porciani, C., Carollo, C. M., & Dekel, A. 2007, MNRAS, 375, 489

- Hahn, O., Carollo, C. M., Porciani, C., & Dekel, A. 2007, MNRAS, 381, 41
- Hahn, O., Teyssier, R., & Carollo, C. M. 2010, MNRAS, 405, 274
- Heavens, A., Refregier, A., & Heymans, C. 2000, MNRAS, 319, 649
- Hilbert, S., Xu, D., Schneider, P., et al. 2017, MNRAS, 468, 790
- Hirv, A., Pelt, J., Saar, E., et al. 2017, A&A, 599, A31
- Hui, L., & Zhang, J. 2008, ApJ, 688, 742
- Joachimi, B., Semboloni, E., Hilbert, S., et al. 2013, MNRAS, 436, 819
- Jones, B. J. T., van de Weygaert, R., & Aragón-Calvo, M. A. 2010, MNRAS, 408, 897
- Kiessling, A., Cacciato, M., Joachimi, B., et al. 2015, Space Sci. Rev., 193, 67
- Kirk, D., Brown, M. L., Hoekstra, H., et al. 2015, Space Sci. Rev., 193, 139
- Klypin, A., Yepes, G., Gottlöber, S., Prada, F., & Heß, S. 2016, MNRAS, 457, 4340
- Joachimi, B., Cacciato, M., Kitching, T. D., et al. 2015, Space Sci. Rev., 193, 1
- Lacerna, I., & Padilla, N. 2012, MNRAS, 426, L26
- Laigle, C., Pichon, C., Codis, S., et al. 2015, MNRAS, 446, 2744
- Lee, J., & Pen, U.-L. 2000, ApJ, 532, L5
- Lee, J., & Pen, U.-L. 2001, ApJ, 555, 106
- Lee, J. 2004, ApJ, 614, L1
- Lee, J., & Erdogdu, P. 2007, ApJ, 671, 1248
- Lee, J., & Pen, U.-L. 2008, ApJ, 681, 798-805
- Lee, J., Hahn, O., & Porciani, C. 2009, ApJ, 707, 761
- Lee, J. 2011, ApJ, 732, 99
- Lee, J., Kim, S., & Rey, S.-C. 2018, ApJ, 860, 127
- Libeskind, N. I., Hoffman, Y., Forero-Romero, J., et al. 2013, MNRAS, 428, 2489
- Navarro, J. F., Abadi, M. G., & Steinmetz, M. 2004, ApJ, 613, L41

- Okumura, T., Nishimichi, T., Umetsu, K., & Osato, K. 2018, *Phys. Rev. D* 98, 023523
- Pandey, B., & Sarkar, S. 2017, *MNRAS*, 467, L6
- Paz, D. J., Stasyszyn, F., & Padilla, N. D. 2008, *MNRAS*, 389, 1127
- Piras, D., Joachimi, B., Schäfer, B. M., et al. 2018, *MNRAS*, 474, 1165
- Planck Collaboration, Ade, P. A. R., Aghanim, N., et al. 2014, *A&A*, 571, A16
- Porciani, C., Dekel, A., & Hoffman, Y. 2002, *MNRAS*, 332, 339
- Press, W. H., Teukolsky, S. A., Vetterling, W. T., & Flannery, B. P. 1992, Cambridge: University Press, —c1992, 2nd ed.,
- Riebe, K., Partl, A. M., Enke, H., et al. 2013, *Astronomische Nachrichten*, 334, 691
- Sheth, R. K., & van de Weygaert, R. 2004, *MNRAS*, 350, 517
- Shi, J., Wang, H., & Mo, H. J. 2015, *ApJ*, 807, 37
- Tempel, E., Stoica, R. S., & Saar, E. 2013, *MNRAS*, 428, 1827
- Tempel, E., & Libeskind, N. I. 2013, *ApJ*, 775, L42
- Tenneti, A., Mandelbaum, R., Di Matteo, T., Feng, Y., & Khandai, N. 2014, *MNRAS*, 441, 470
- Tenneti, A., Mandelbaum, R., Di Matteo, T., Kiessling, A., & Khandai, N. 2015, *MNRAS*, 453, 469
- Troxel, M. A., & Ishak, M. 2015, *Phys. Rep.*, 558, 1
- Trowland, H. E., Lewis, G. F., & Bland-Hawthorn, J. 2013, *ApJ*, 762, 72
- Trujillo, I., Carretero, C., & Patiri, S. G. 2006, *ApJ*, 640, L111
- Tugendhat, T. M., & Schäfer, B. M. 2018, *MNRAS*, 476, 3460
- Veena, G. P., Cautun, M., van de Weygaert, R., et al. 2018, arXiv:1805.00033
- Wall, J. V., & Jenkins, C. R. 2012, *Practical Statistics for Astronomers*, (Cambridge, UK: Cambridge University Press)
- Wang, H., Mo, H. J., Jing, Y. P., Yang, X., & Wang, Y. 2011, *MNRAS*, 413, 1973

- Wang, P., & Kang, X. 2017, MNRAS, 468, L123
- Welker, C., Devriendt, J., Dubois, Y., Pichon, C., & Peirani, S. 2014, MNRAS, 445, L46
- White, S. D. M. 1984, ApJ, 286, 38
- Xia, Q., Kang, X., Wang, P., et al. 2017, ApJ, 848, 22
- Zhang, Y., Yang, X., Faltenbacher, A., et al. 2009, ApJ, 706, 747
- Zhang, Y., Yang, X., Wang, H., et al. 2013, ApJ, 779, 160
- Zhang, Y., Yang, X., Wang, H., et al. 2015, ApJ, 798, 17
- Zel'dovich, Y. B. 1970, A&A, 5, 84

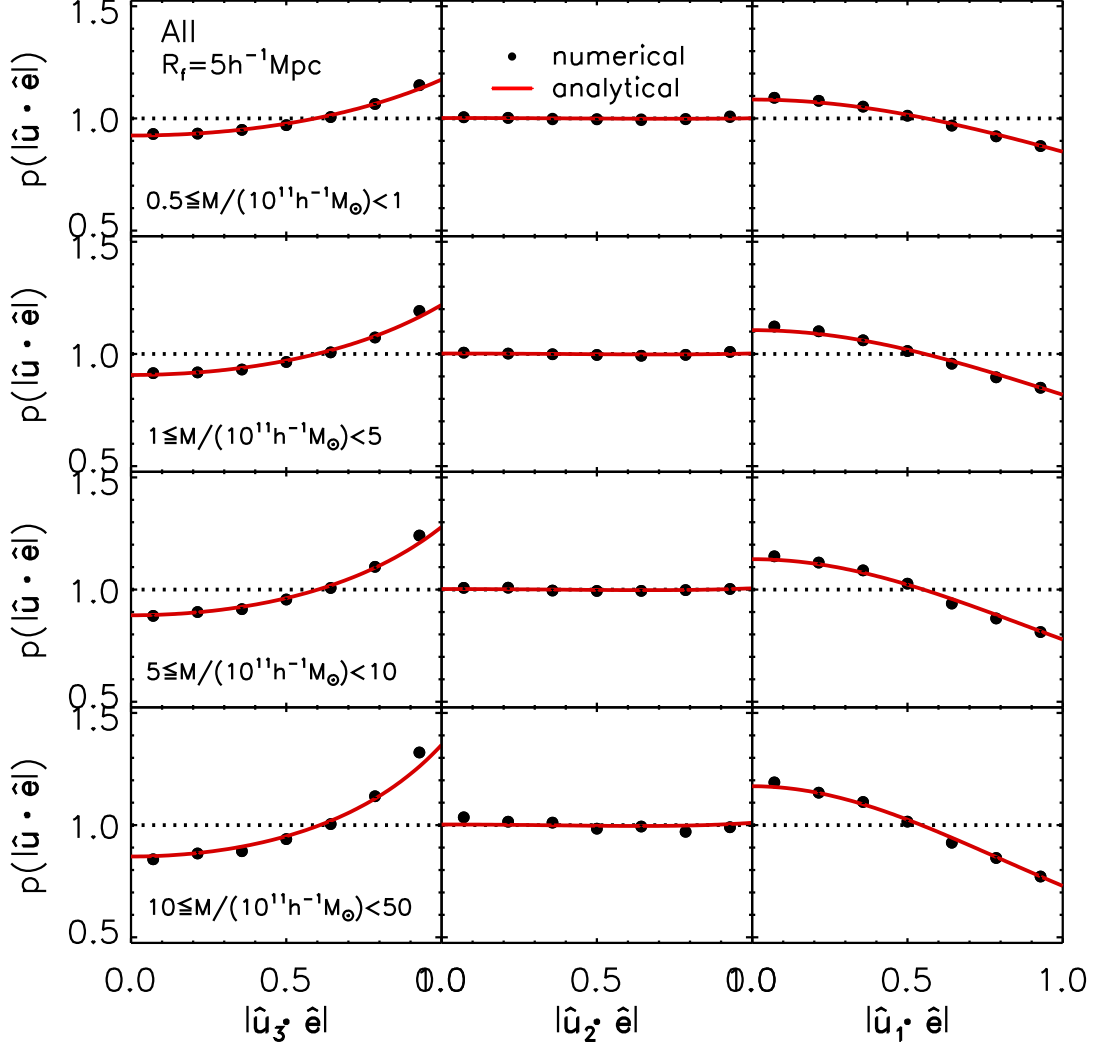


Fig. 1.— Probability density distributions of three coordinates of the unit shape vectors, \hat{e} , of the lowest-mass (top panel), low-mass (first middle panel), medium-mass (second middle panel) and high-mass (bottom panel) galactic halos in the principal frame spanned by the minor ($\hat{\mathbf{u}}_3$), intermediate ($\hat{\mathbf{u}}_2$), and major ($\hat{\mathbf{u}}_1$) eigenvectors of the tidal fields smoothed on the scale of $R_f = 5 h^{-1} \text{Mpc}$. In each panel, the numerical results are plotted as black filled circular dots with Poisson errors, while the analytic model, Equations (1)-(4), with the empirically determined value of d_t is shown as red solid line. The uniform constant probability density is depicted as black dotted line.

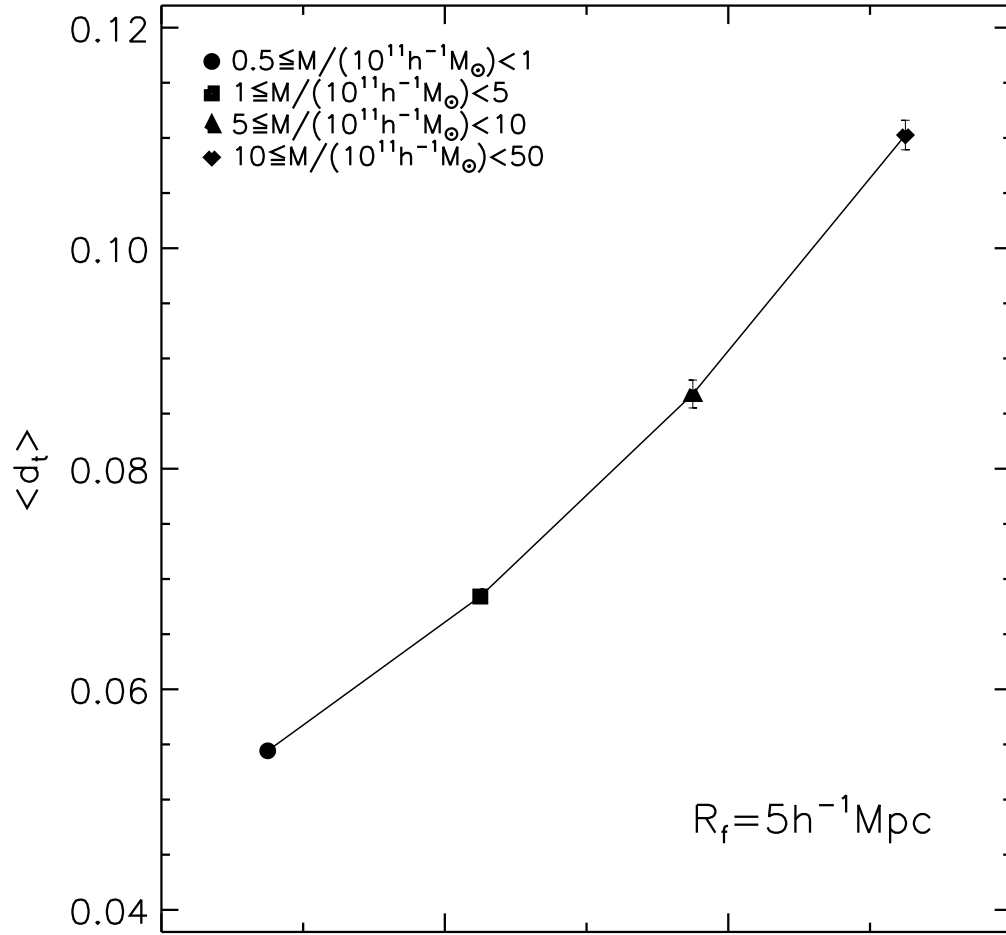


Fig. 2.— Mean values of the shape correlation parameter d_t averaged over the galactic halos belonging to four different mass ranges when the local tidal fields are smoothed on the scale of $R_f = 5 h^{-1} \text{Mpc}$.

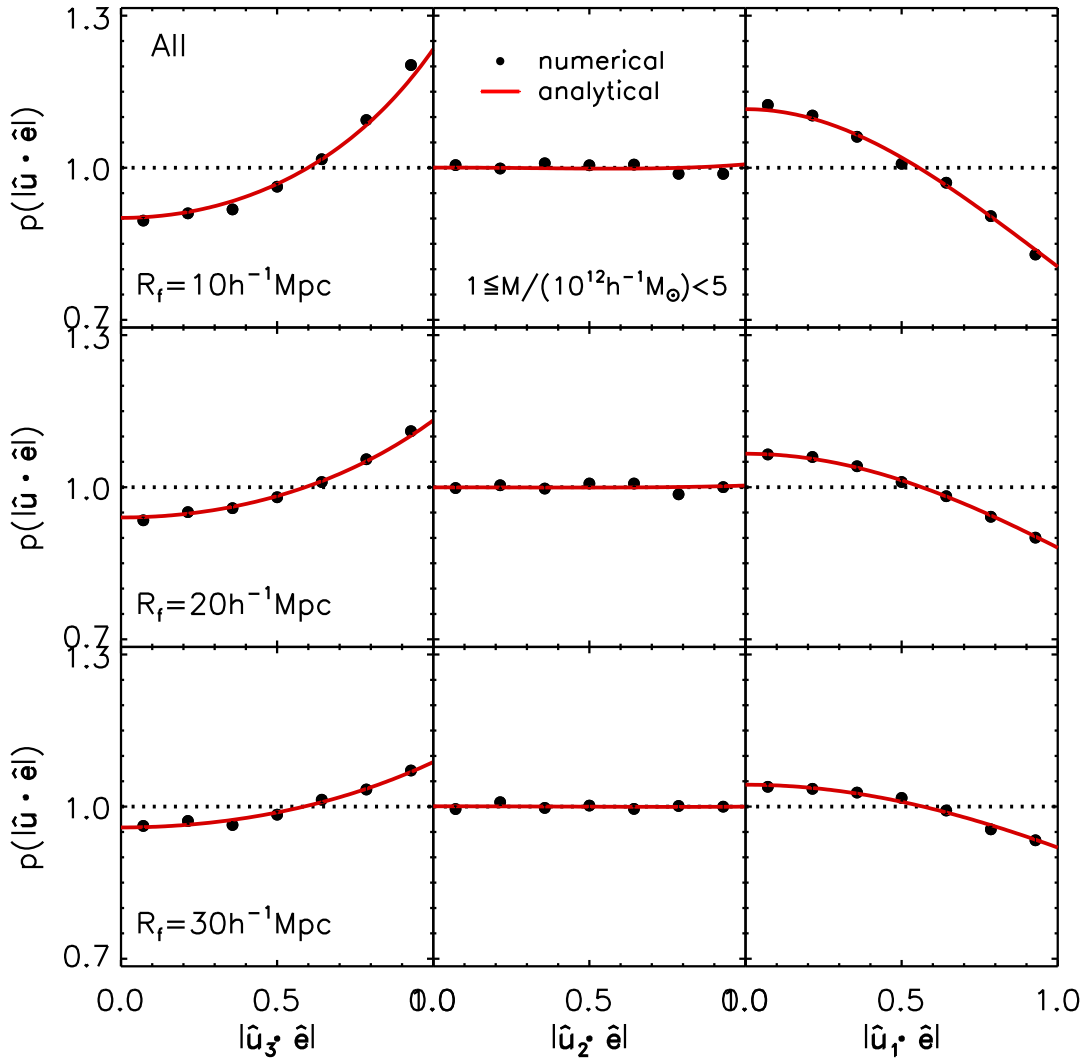


Fig. 3.— Same as the bottom panels of Figure 1 but for the cases of three larger smoothing scales of $R_f = 10, 20, 30 h^{-1} \text{Mpc}$.

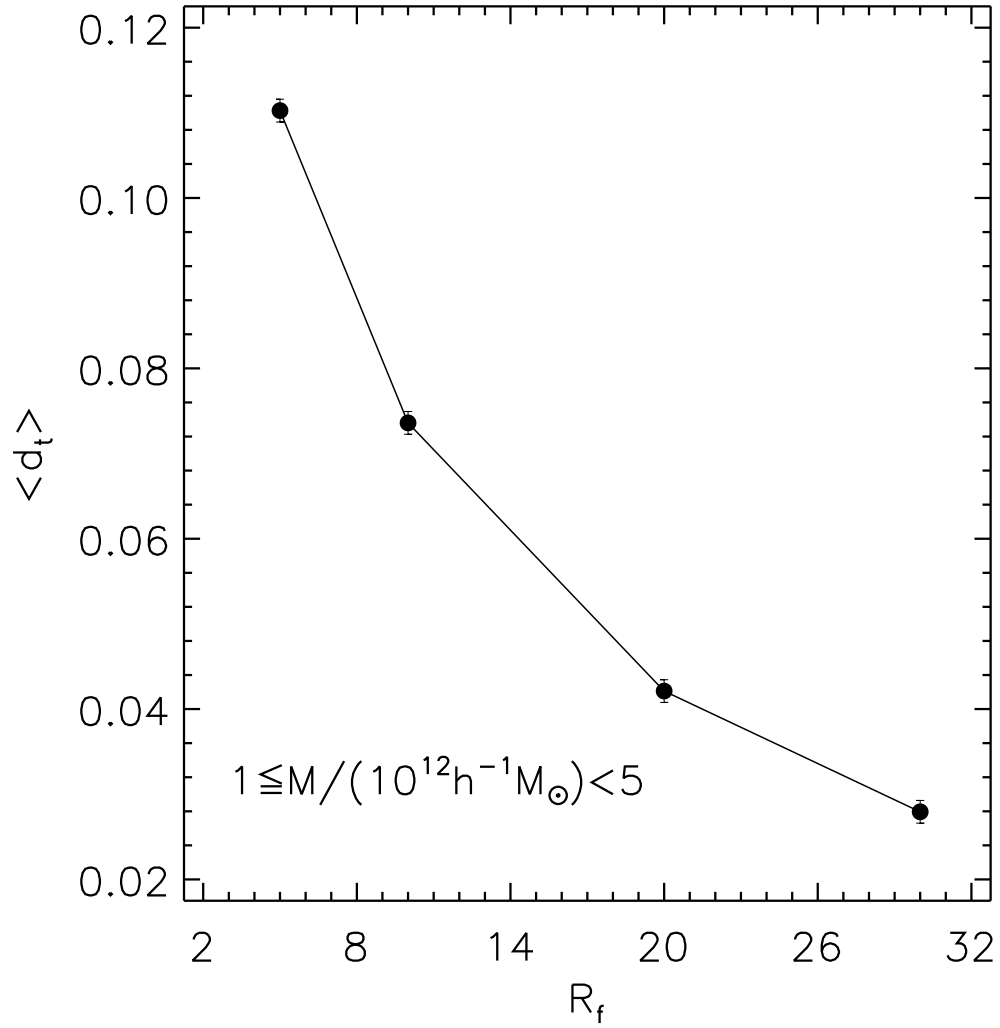


Fig. 4.— Mean values of the shape correlation parameter d_t averaged over the high-mass galactic halos as a function of the smoothing scale, R_f .

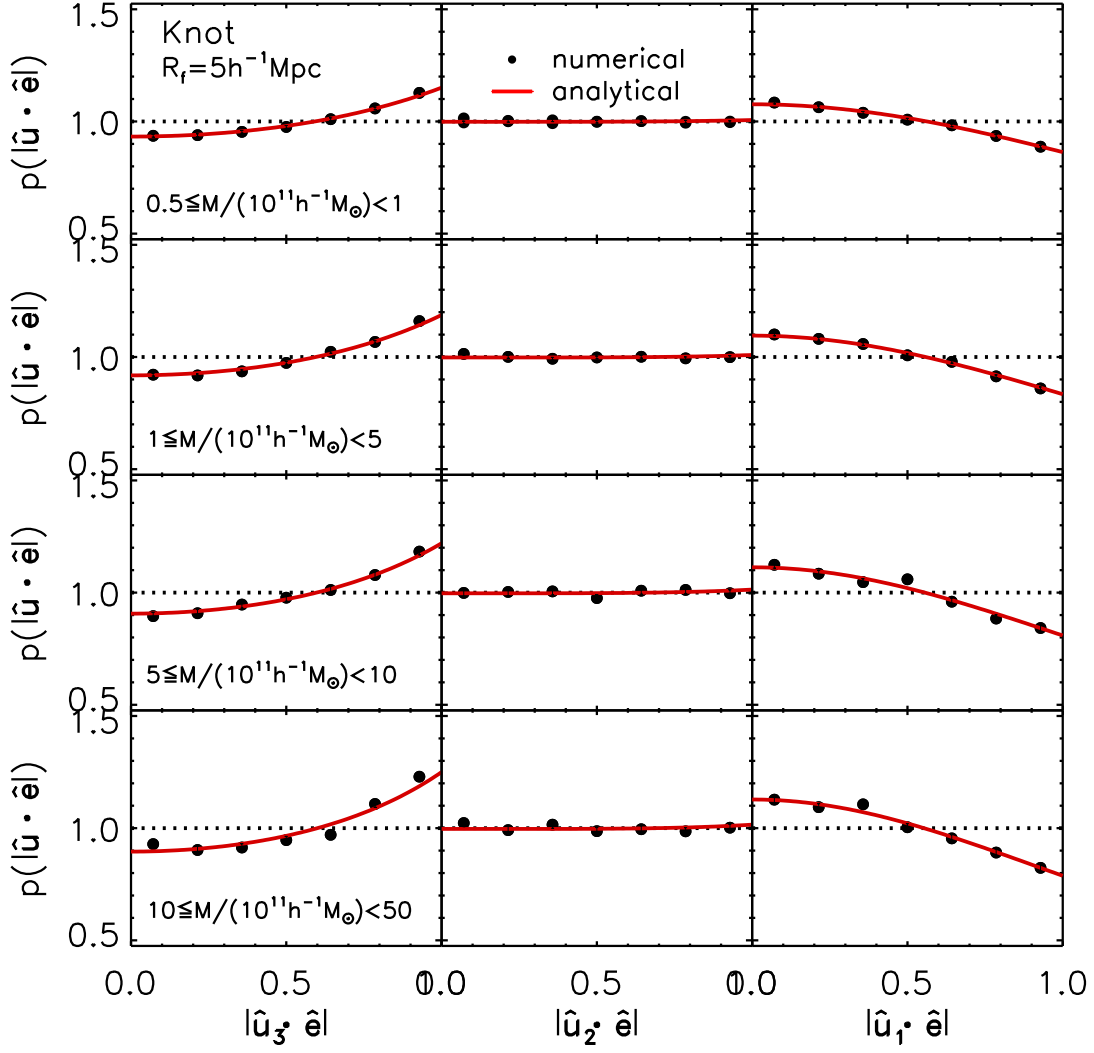


Fig. 5.— Same as Figure 1 but with only those galactic halos located in the knot environments where all three eigenvalues of the tidal fields, λ_1 , λ_2 , λ_3 , are positive.

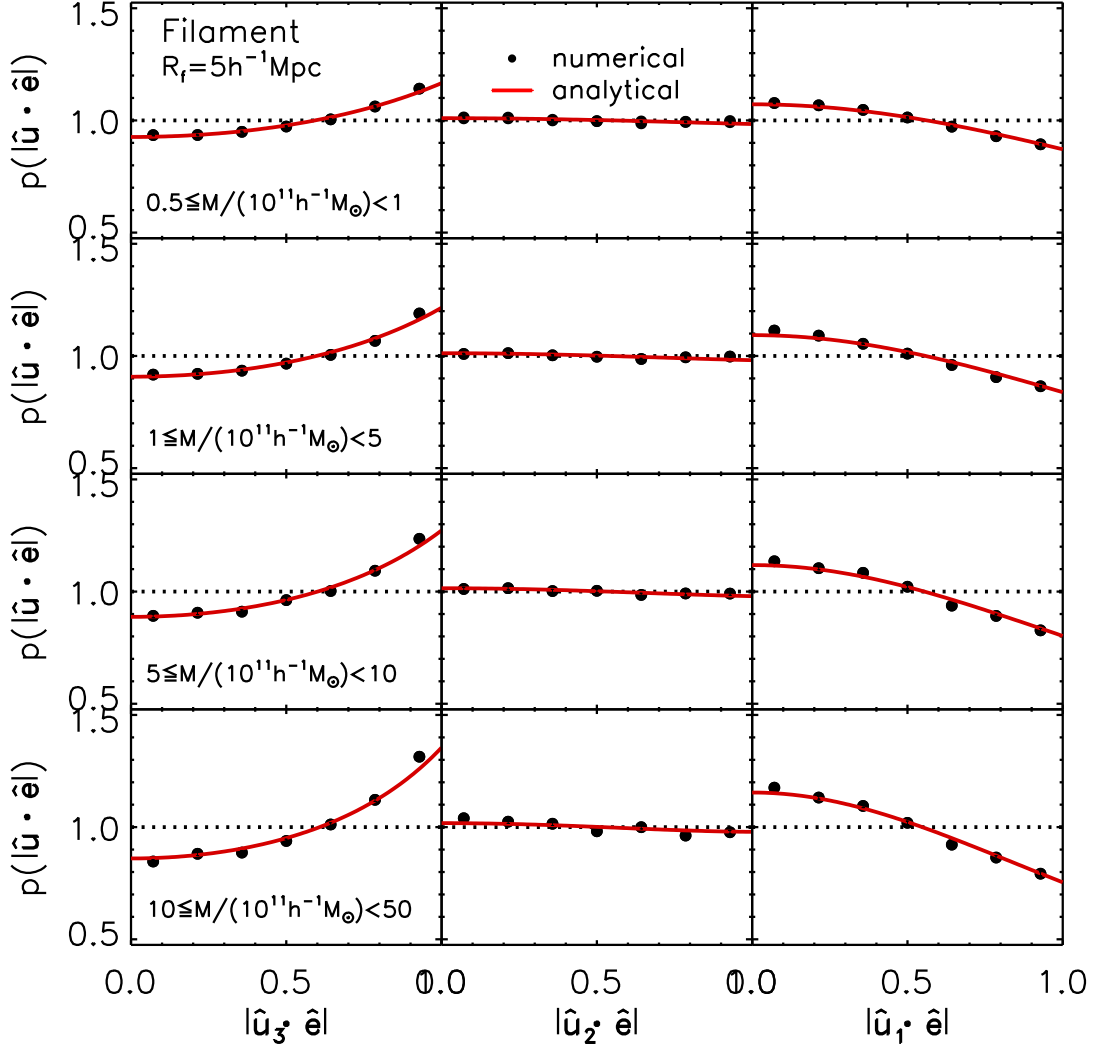


Fig. 6.— Same as Figure 1 but with only those galactic halos located in the filament environments where $\lambda_1 > \lambda_2 > 0 > \lambda_3$.

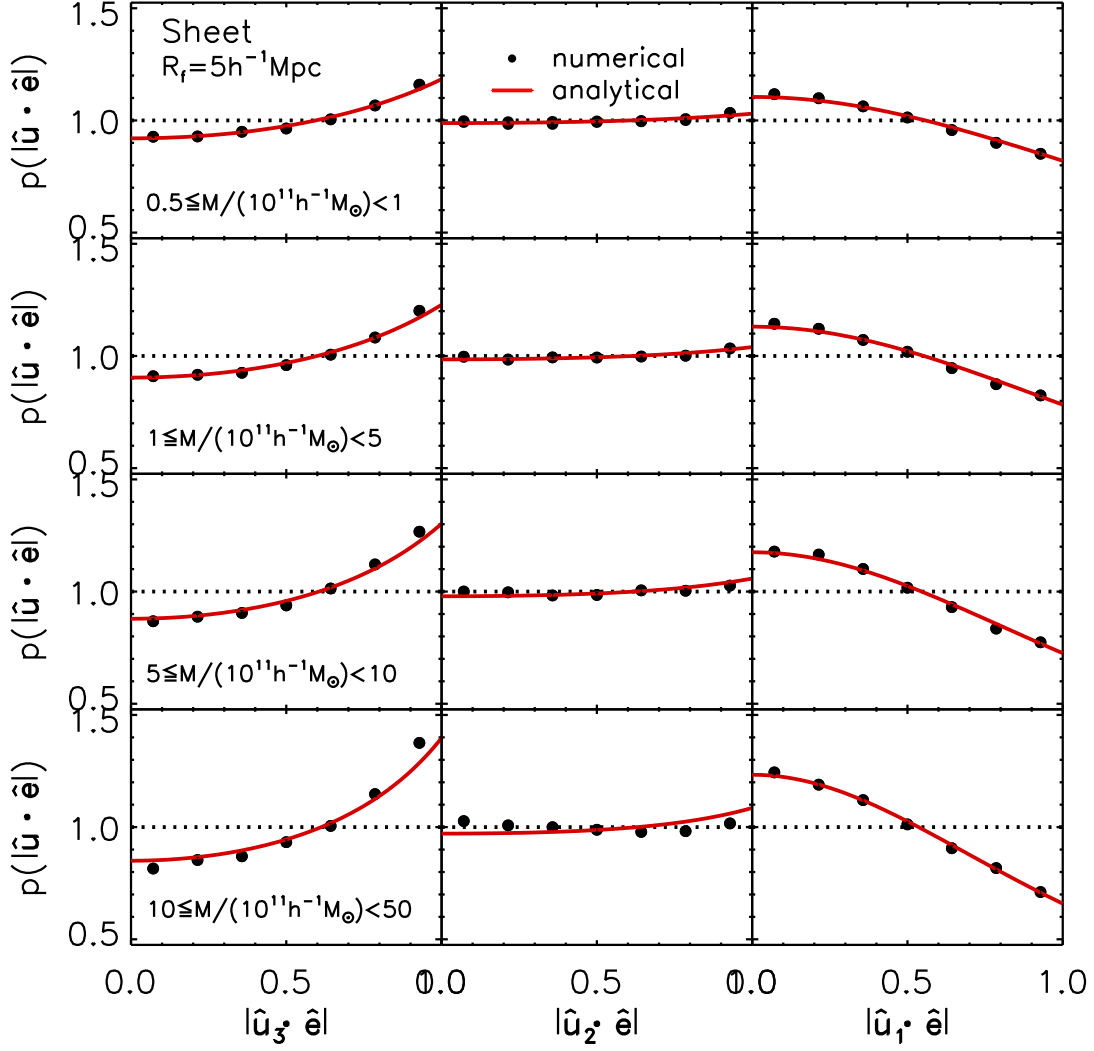


Fig. 7.— Same as Figure 1 but with only those galactic halos located in the sheet environments where $\lambda_1 > 0 > \lambda_2 > \lambda_3$.

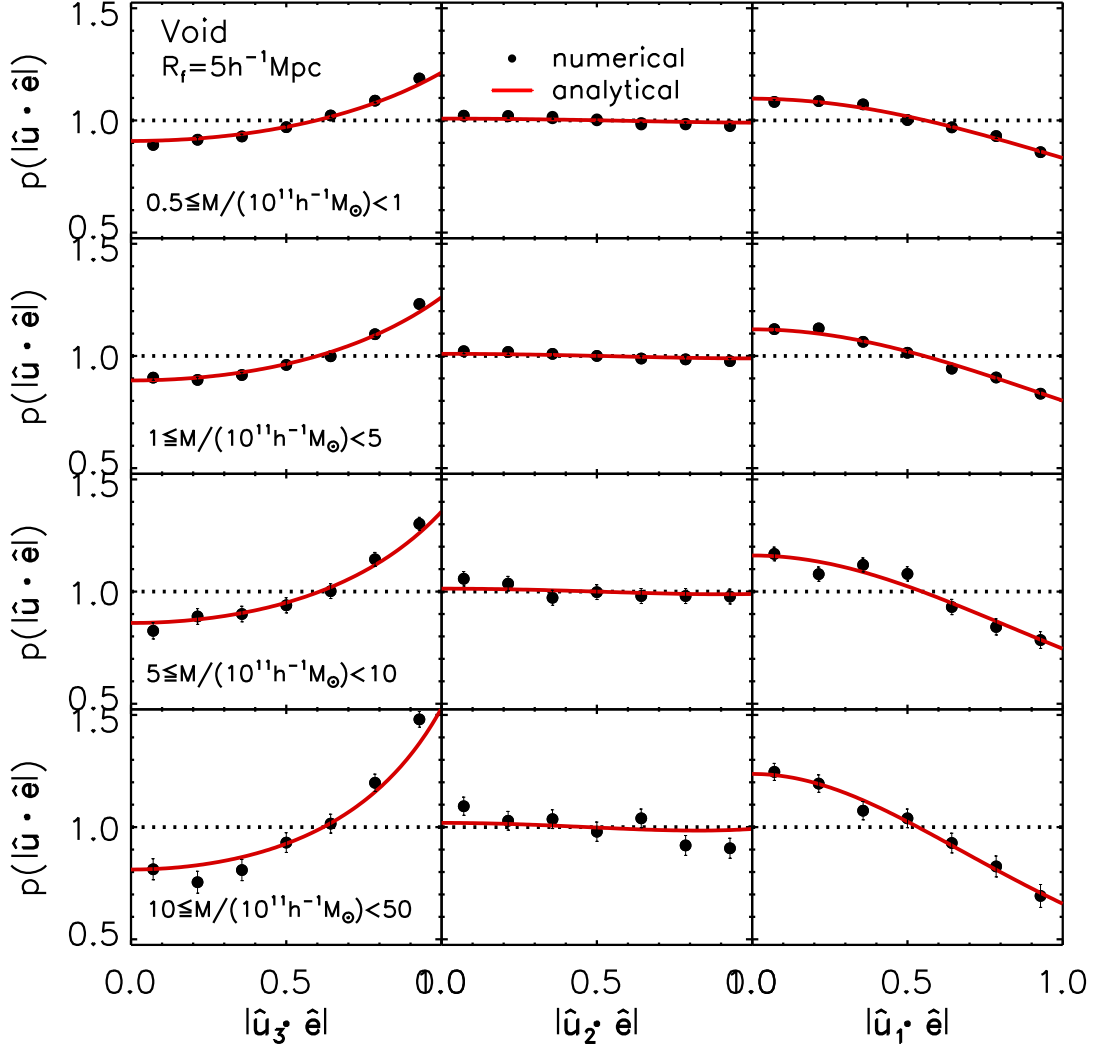


Fig. 8.— Same as Figure 1 but with only those galactic halos located in the void environments where $0 > \lambda_1 > \lambda_2 > \lambda_3$.

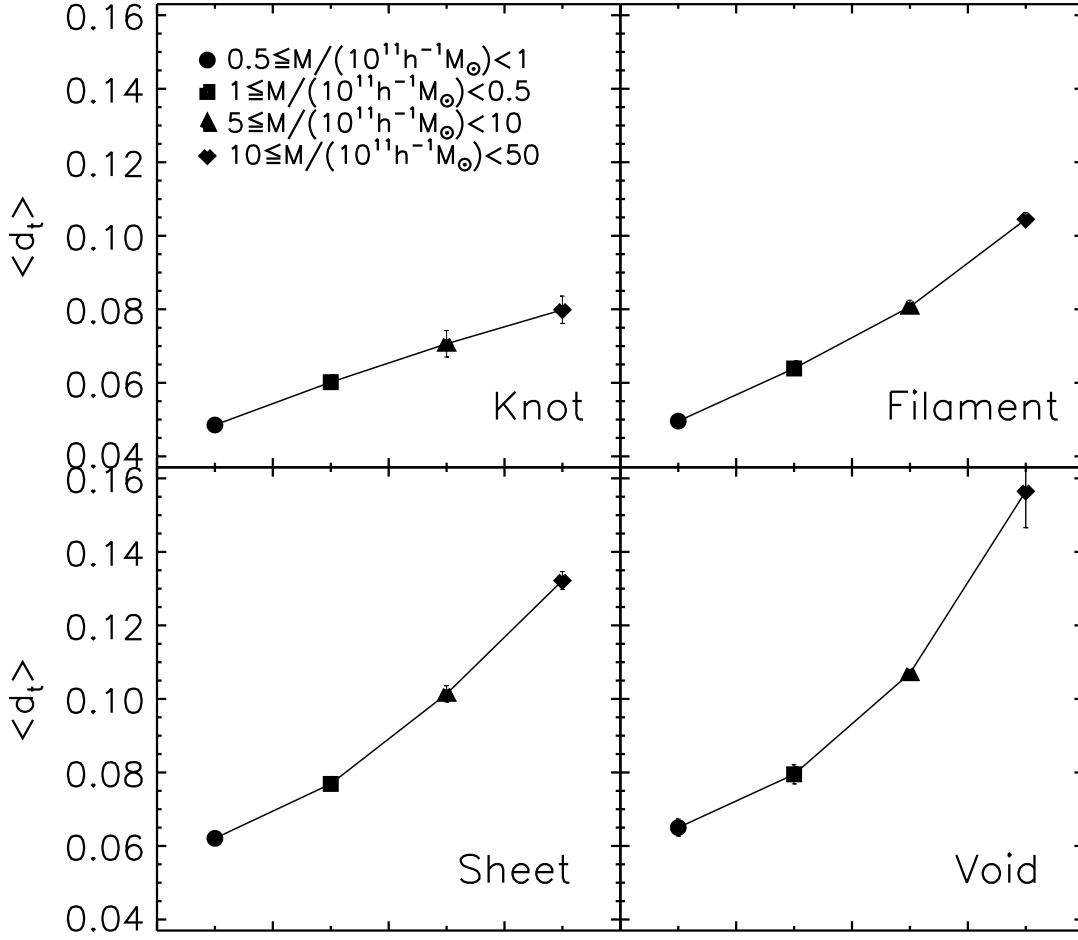


Fig. 9.— Same as Figure 2 but with those galactic halos embedded in four different types of the cosmic web.

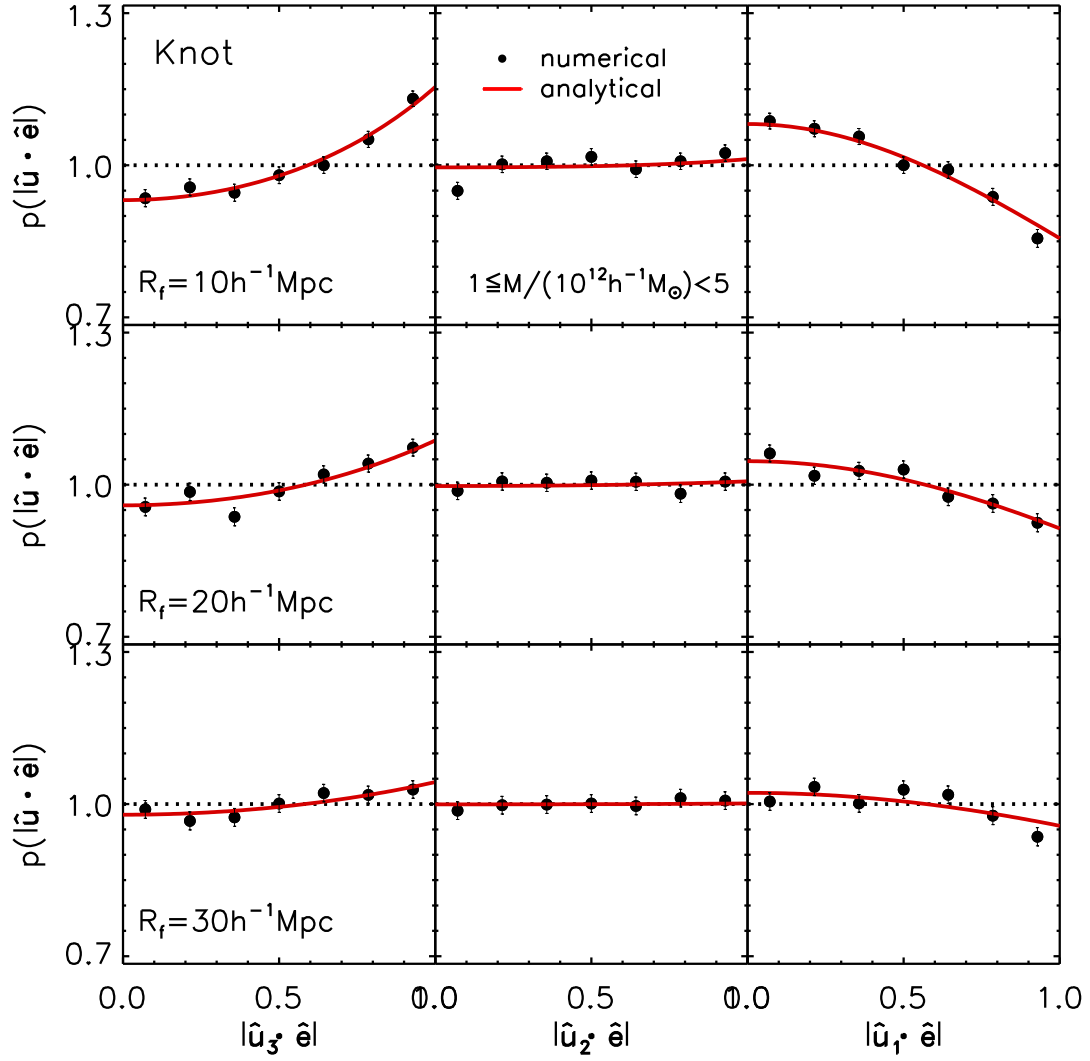


Fig. 10.— Same as Figure 3 but with only those galactic halos located in the knot environments.

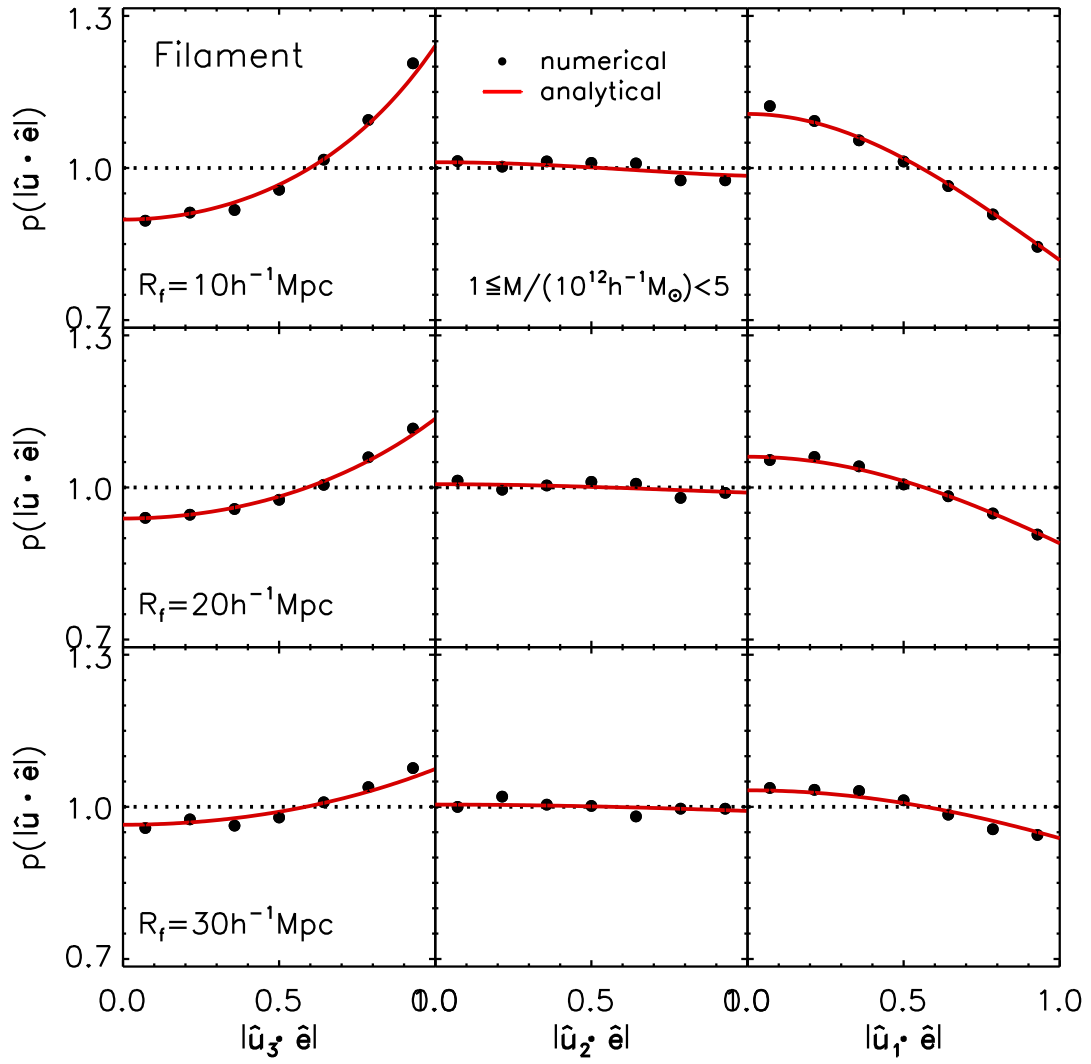


Fig. 11.— Same as Figure 3 but with only those galactic halos located in the filament environments where $\lambda_1 > \lambda_2 > 0 > \lambda_3$.

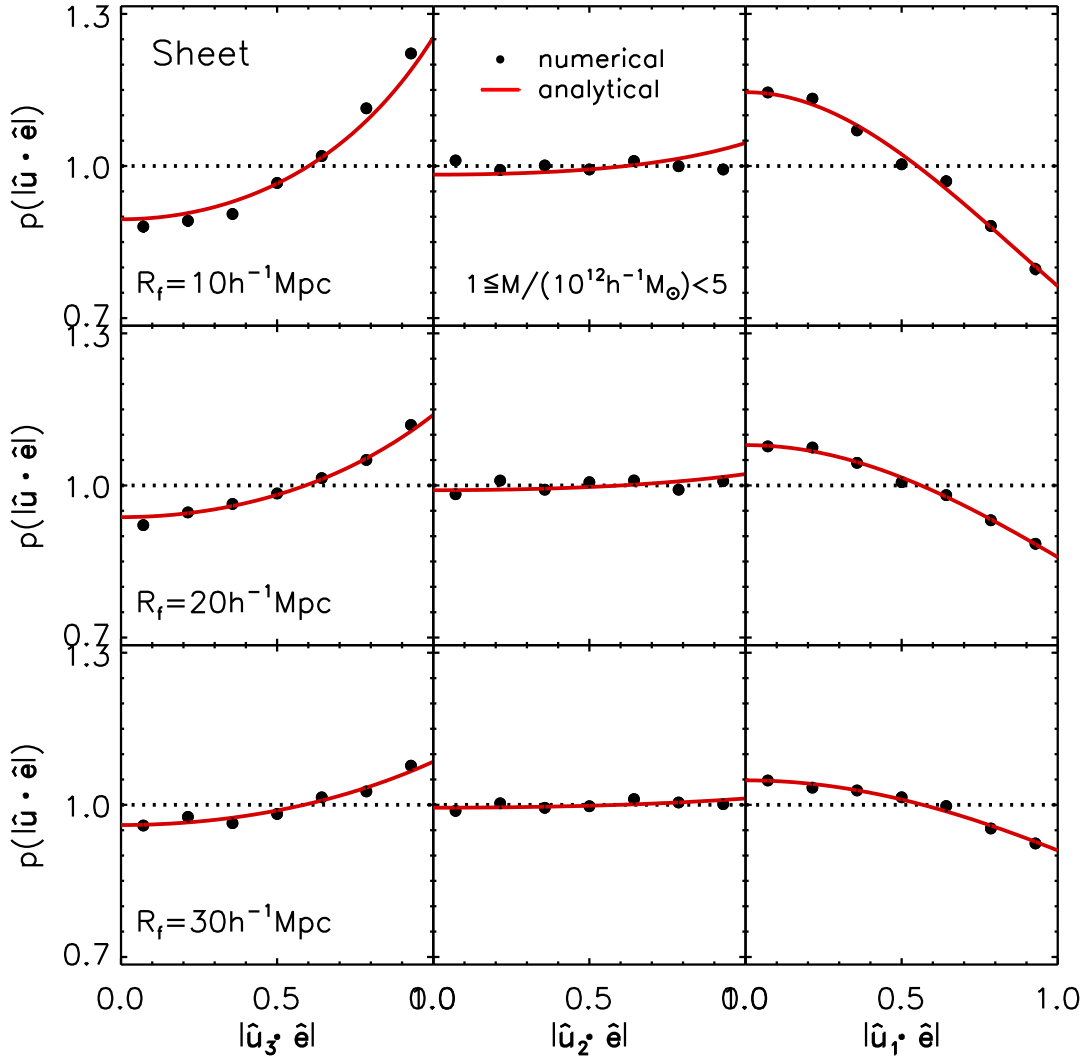


Fig. 12.— Same as Figure 3 but with only those galactic halos located in the sheet environments where $\lambda_1 > 0 > \lambda_2 > \lambda_3$.

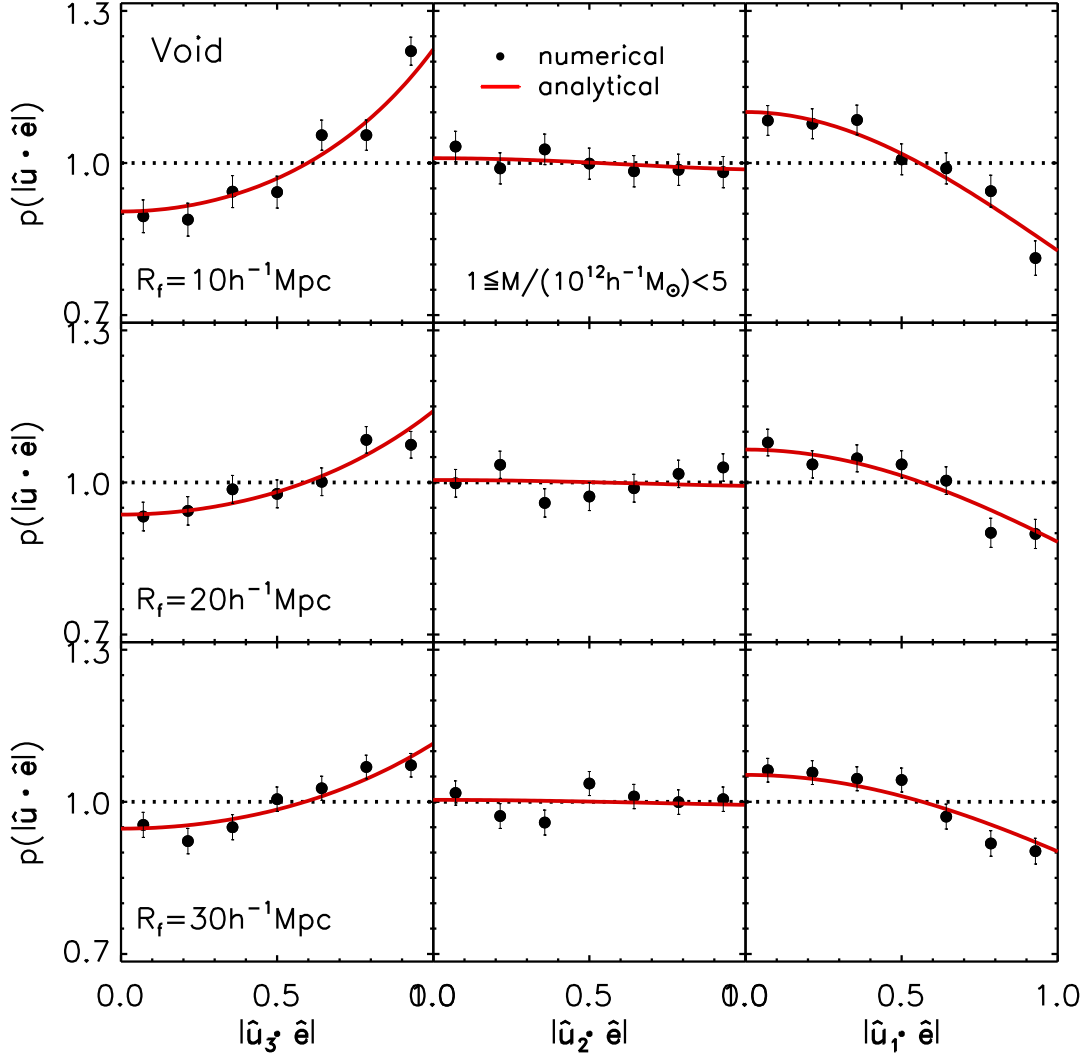


Fig. 13.— Same as Figure 3 but with only those galactic halos located in the void environments where $0 > \lambda_1 > \lambda_2 > \lambda_3$.

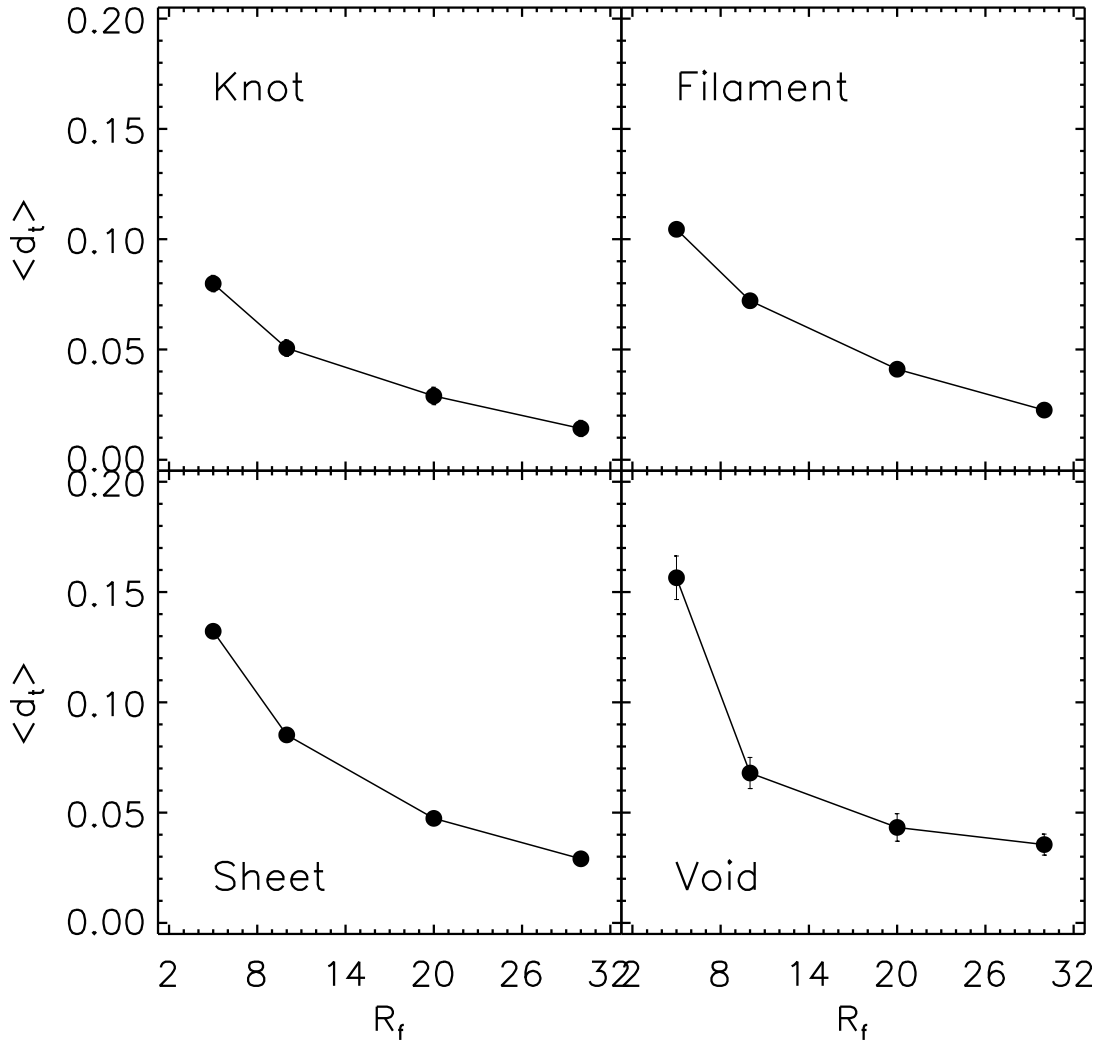


Fig. 14.— Mean values of the shape correlation parameter averaged over the high-mass galactic halos belonging to the four different types of the cosmic web versus the smoothing scale R_f .

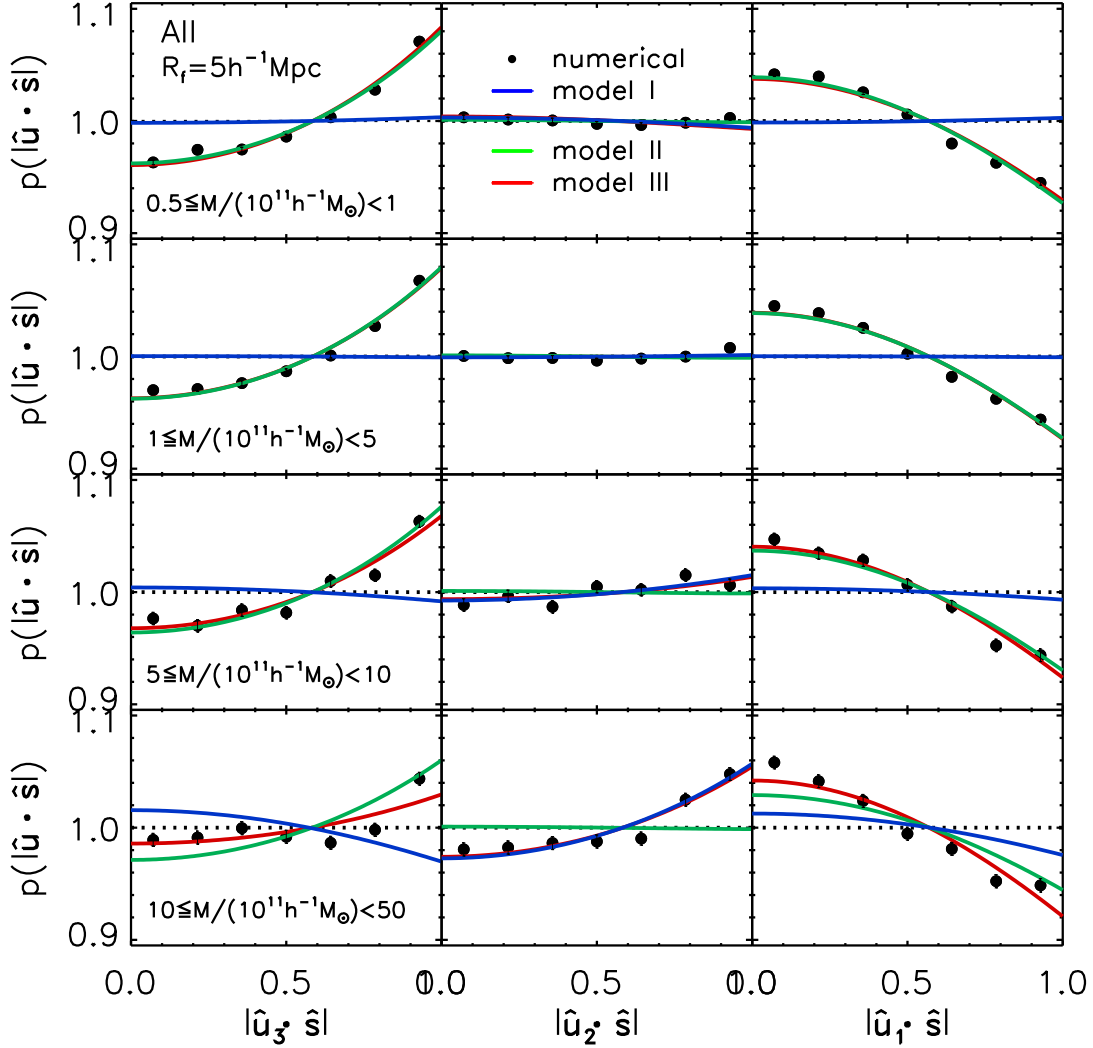


Fig. 15.— Probability density distributions of three coordinates of the unit spin vectors, \hat{s} , of the galactic halos in the principal frame spanned by three eigenvectors, $\{\hat{\mathbf{u}}_1, \hat{\mathbf{u}}_2, \hat{\mathbf{u}}_3\}$, of the local tidal fields smoothed on the scale of $R_f = 5 h^{-1} \text{Mpc}$, for four different ranges of the halo mass M . In each panel, the numerical results are plotted as black filled circular dots while the analytic model with the empirically determined parameters is shown as red solid line. The uniform probability density is depicted as black dotted line.

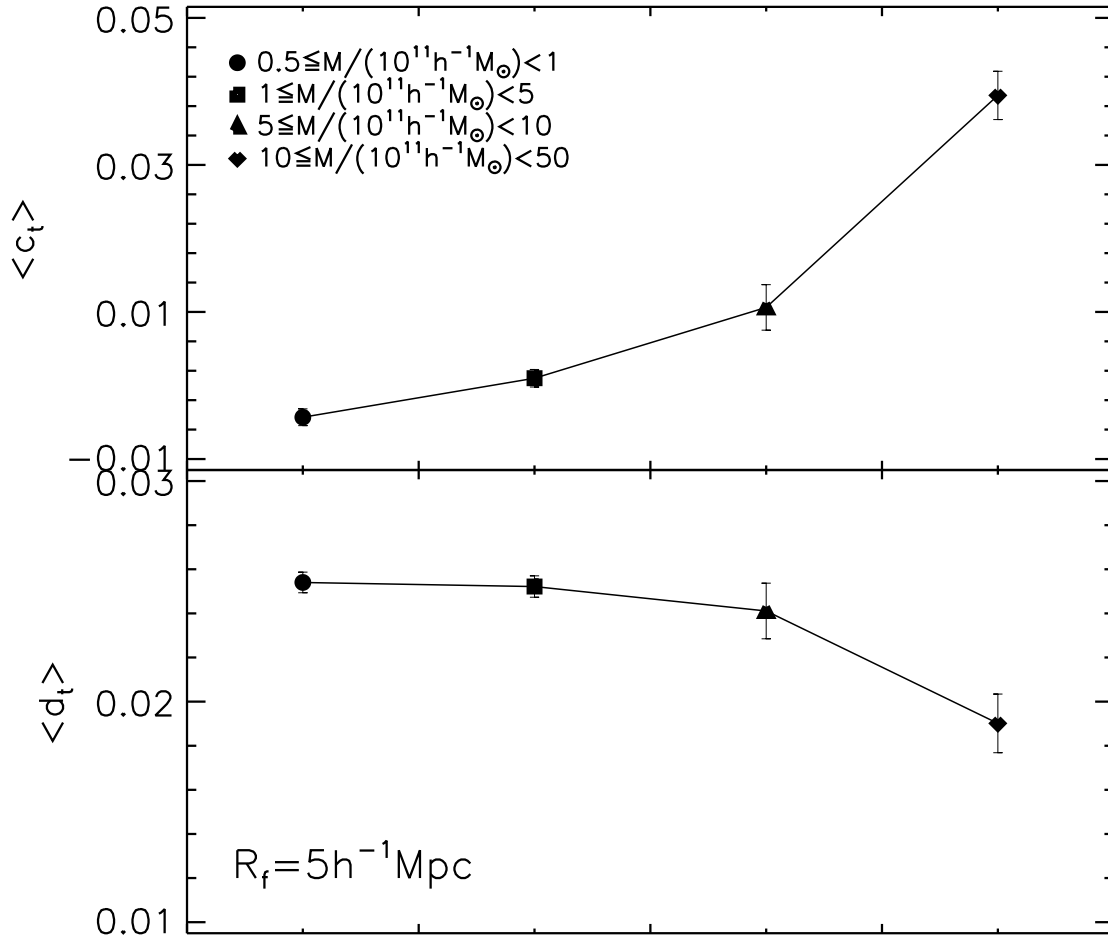


Fig. 16.— Mean values of the first and second spin correlation parameters, c_t and d_t , averaged over the galactic halos belonging to four different mass ranges for the case of $R_f = 5 h^{-1} \text{Mpc}$ in the top and bottom panels, respectively.

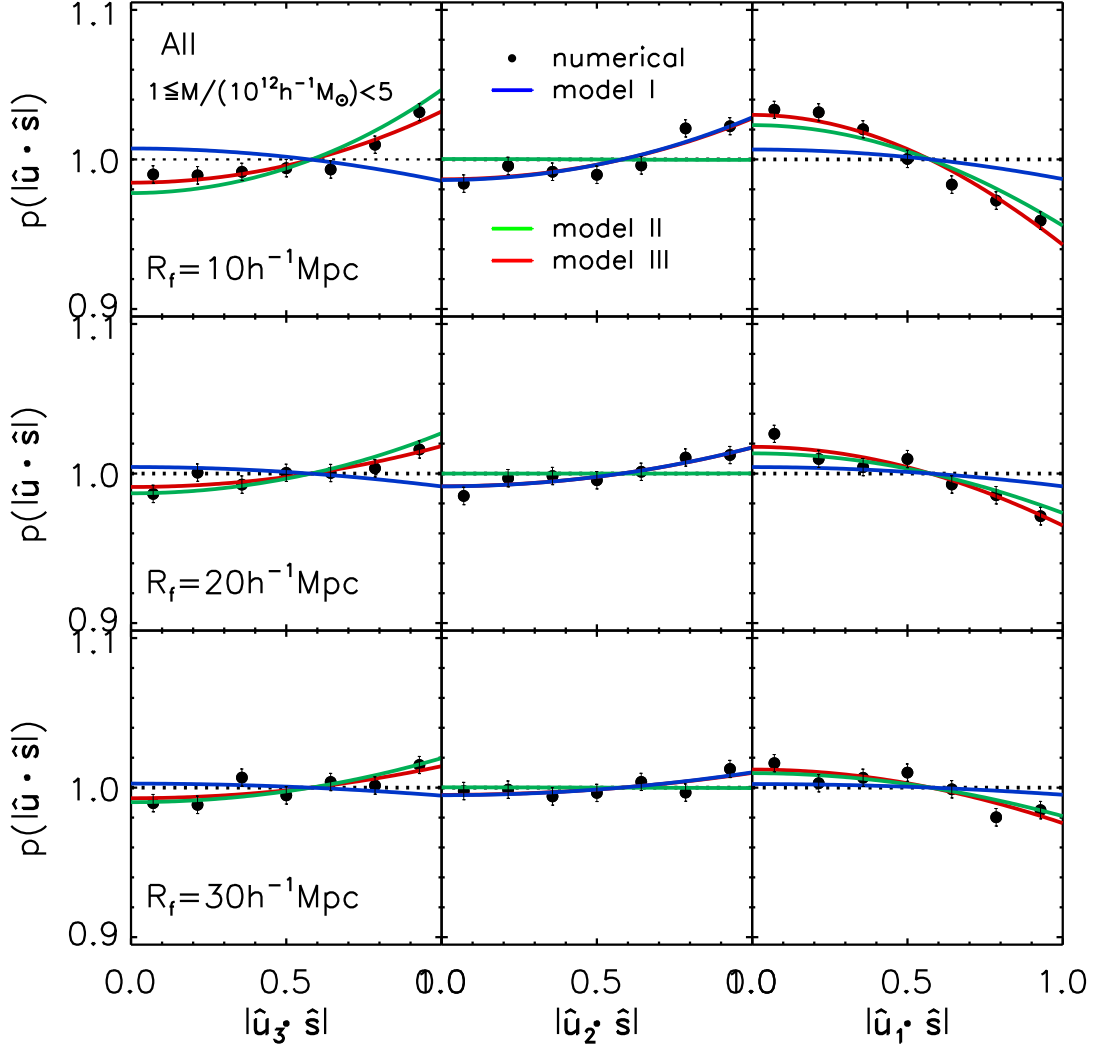


Fig. 17.— Probability density distributions, $p(|\hat{\mathbf{u}}_3 \cdot \hat{\mathbf{e}}|)$, $p(|\hat{\mathbf{u}}_2 \cdot \hat{\mathbf{e}}|)$, $p(|\hat{\mathbf{u}}_1 \cdot \hat{\mathbf{e}}|)$ of the high-mass galactic halos for three different cases of the smoothing scale R_f .

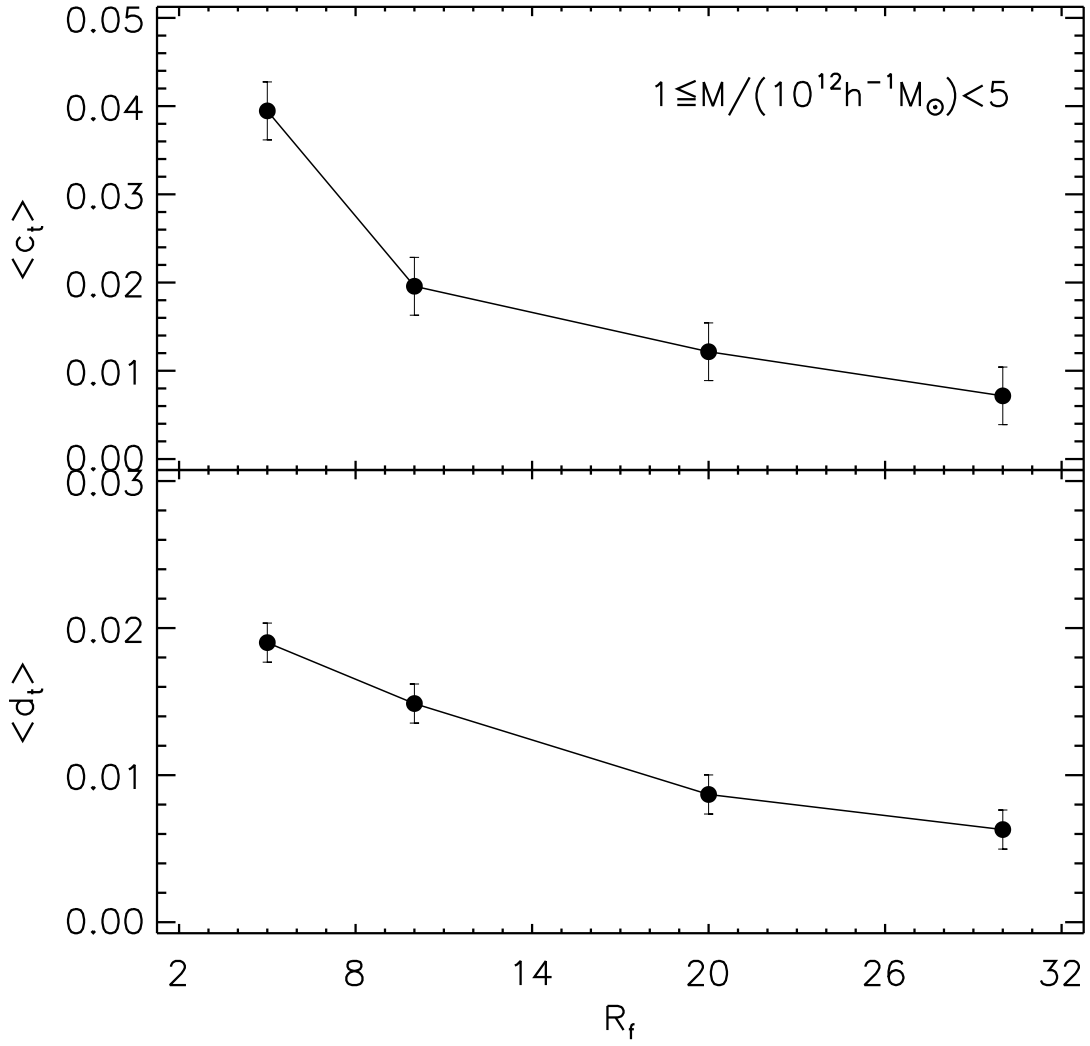


Fig. 18.— Mean values of the first and second spin correlation parameters, c_t and d_t , averaged over the high-mass galactic halos as a function of R_f in the top and bottom panels, respectively.

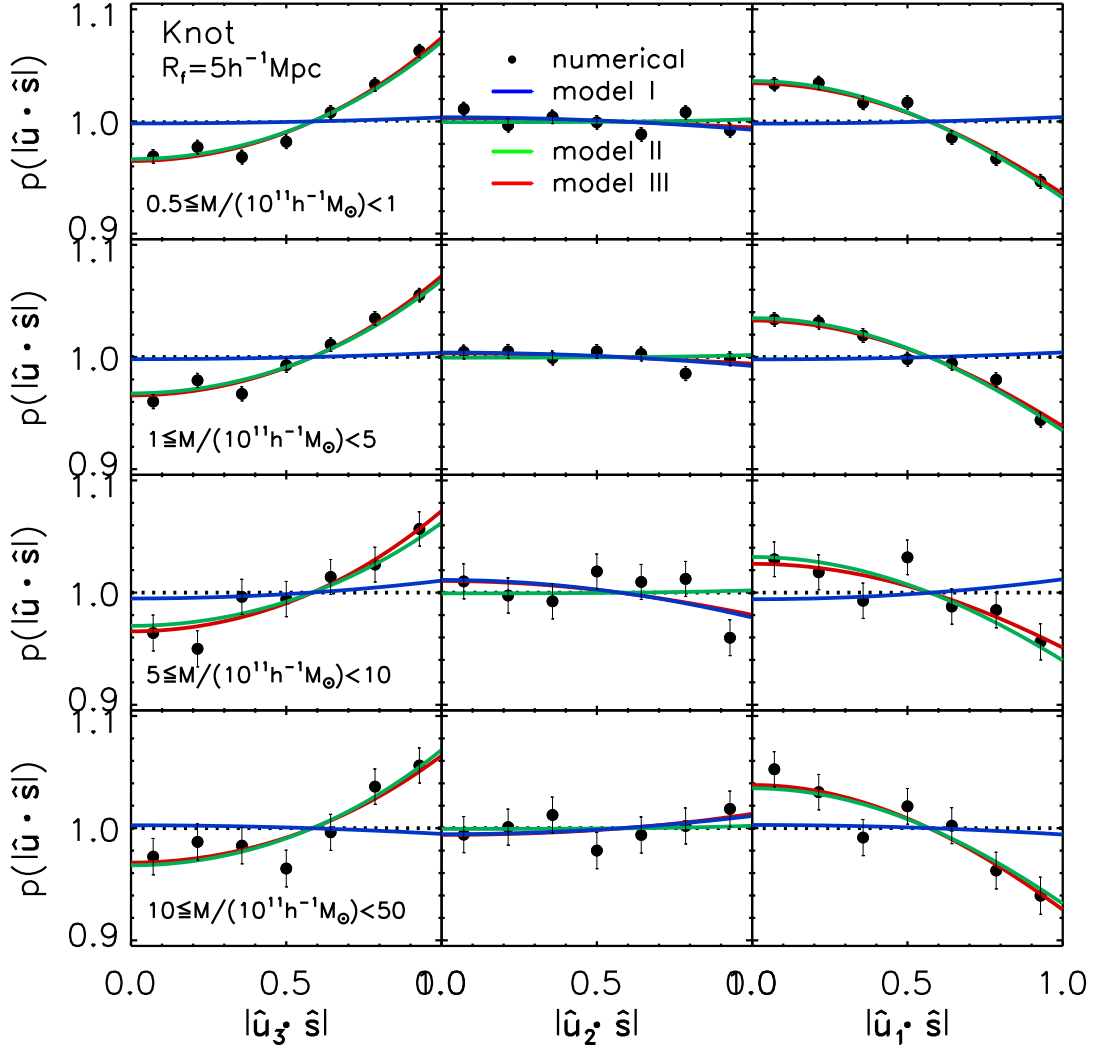


Fig. 19.— Same as Figure 15 but with only those galactic halos located in the knot environments where all three eigenvalues of the local tidal fields, λ_1 , λ_2 , λ_3 , are positive.

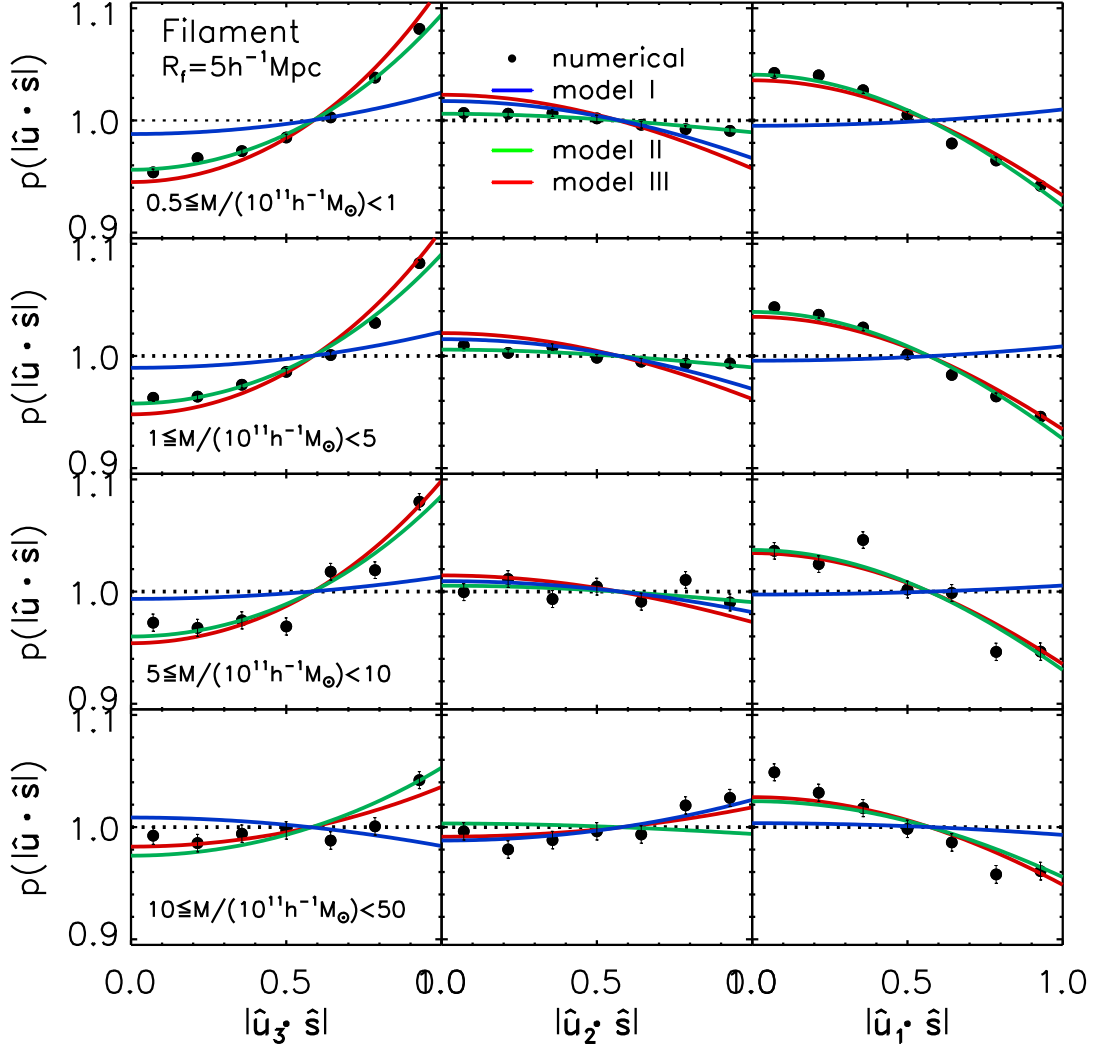


Fig. 20.— Same as Figure 15 but with only those galactic halos located in the filament environments where $\lambda_1 > \lambda_2 > 0 > \lambda_3$.

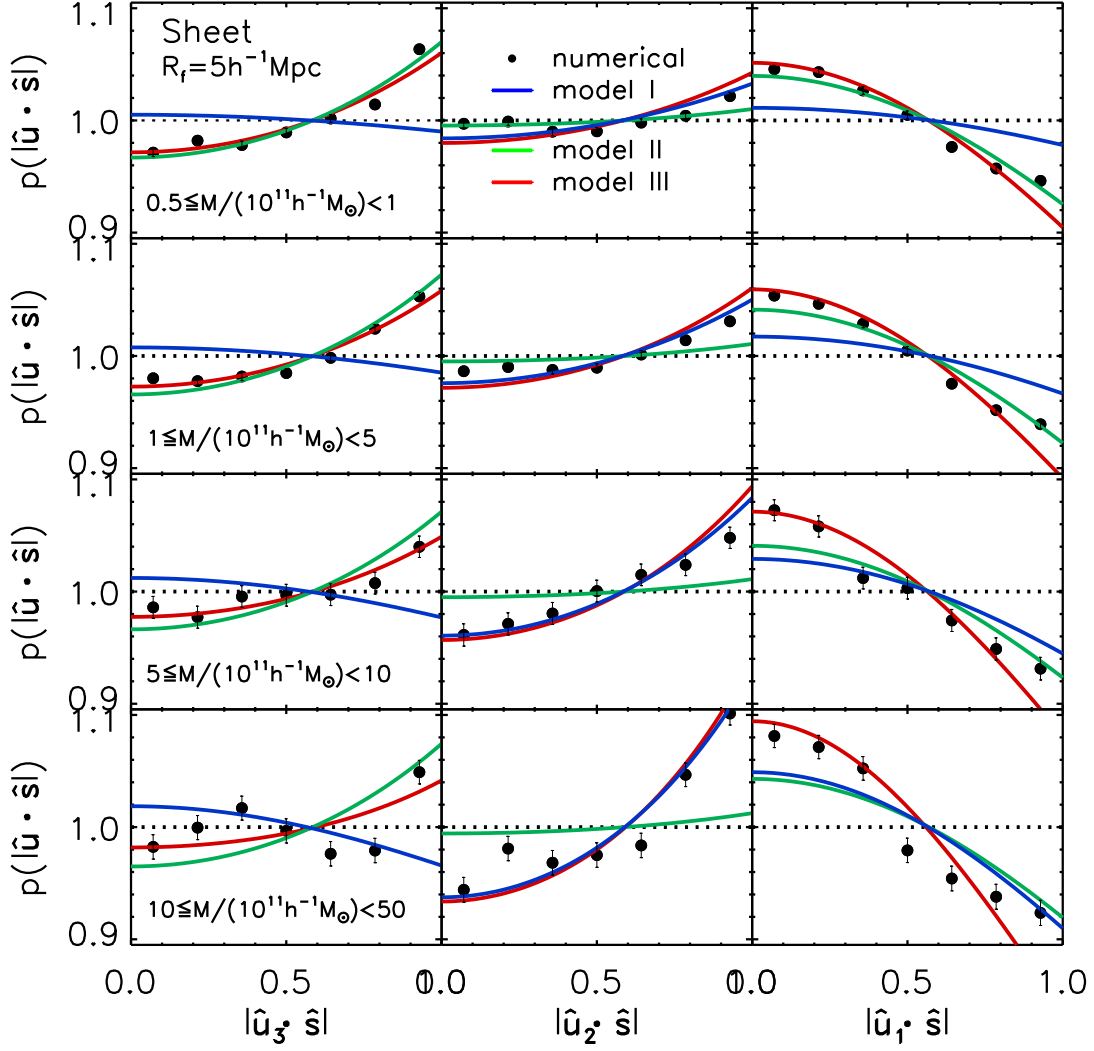


Fig. 21.— Same as Figure 15 but with only those galactic halos located in the sheet environments where $\lambda_1 > 0 > \lambda_2 > \lambda_3$.

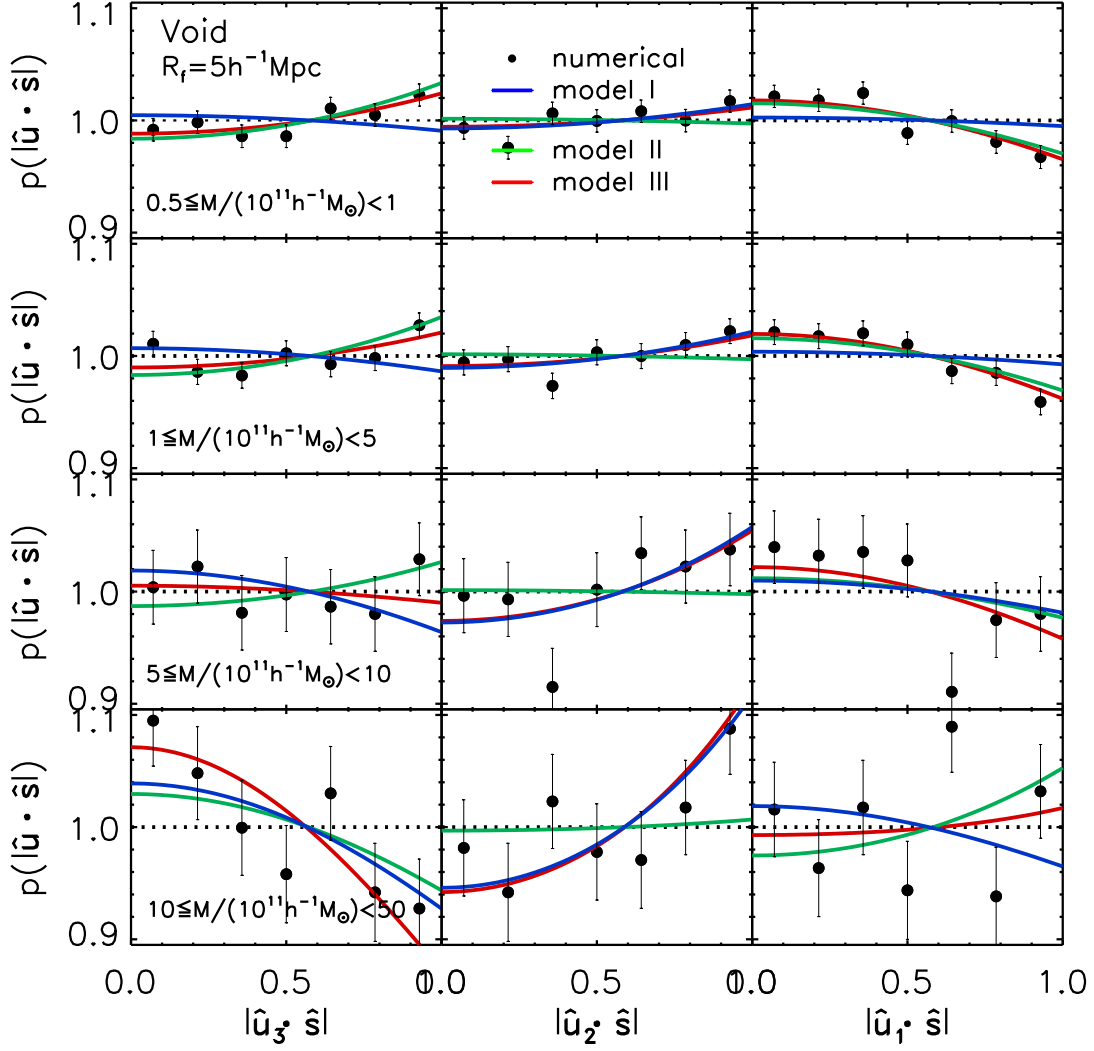


Fig. 22.— Same as Figure 15 but with only those galactic halos located in the void environments where $0 > \lambda_1 > \lambda_2 > \lambda_3$.

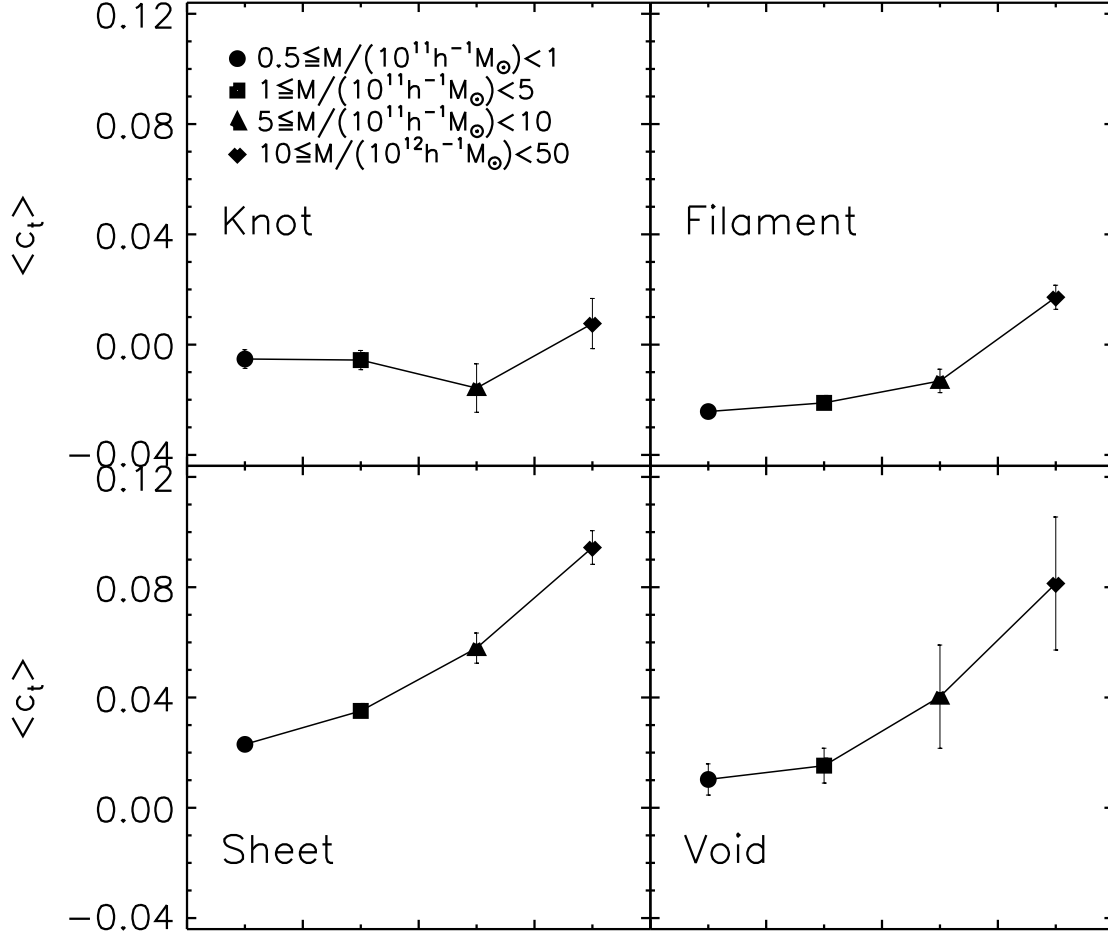


Fig. 23.— Mean values of the first spin correlation parameter c_t averaged over the knot (top-left panel), filament (top-right panel), sheet (bottom-left panel), and void (bottom-right panel) galactic halos in four different mass ranges. The smoothing scale R_f is set at $5 h^{-1} \text{Mpc}$.

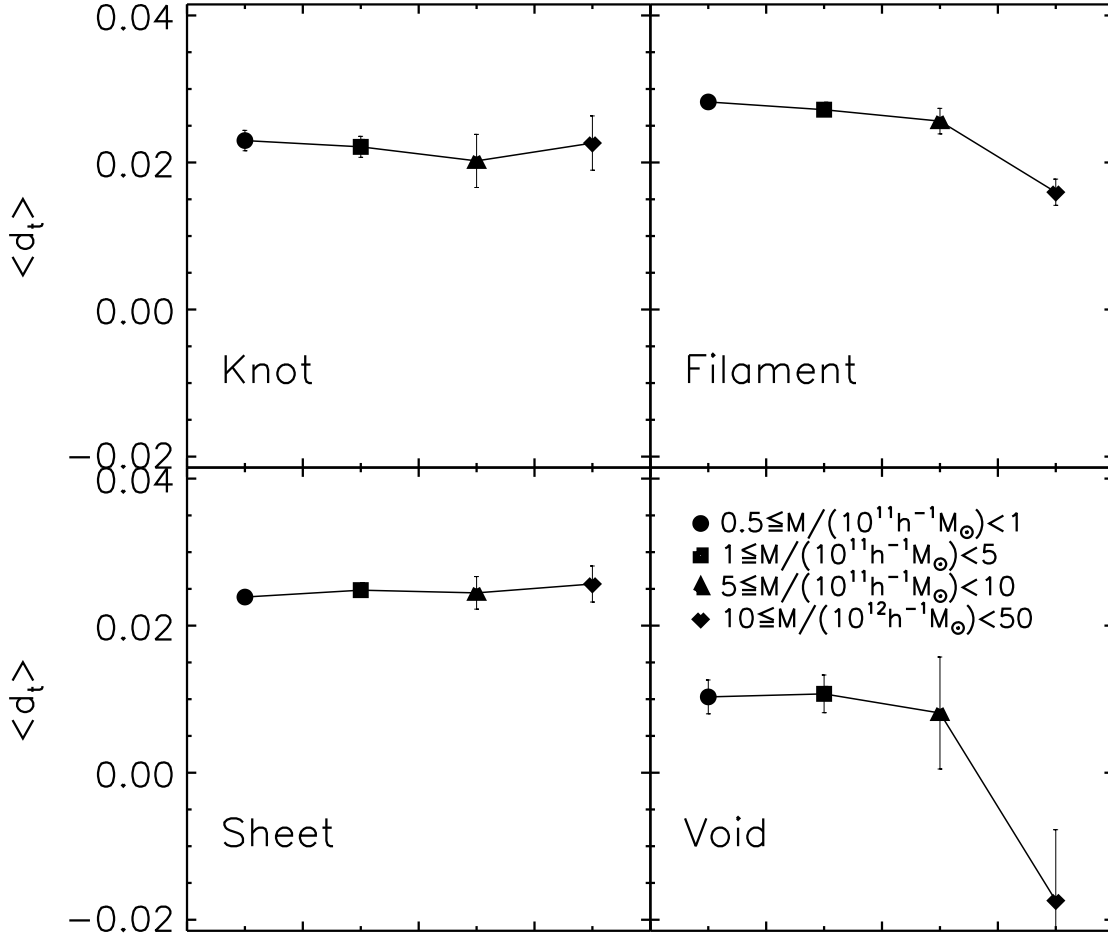


Fig. 24.— Same as Figure 23 but for the second spin correlation parameter d_t .

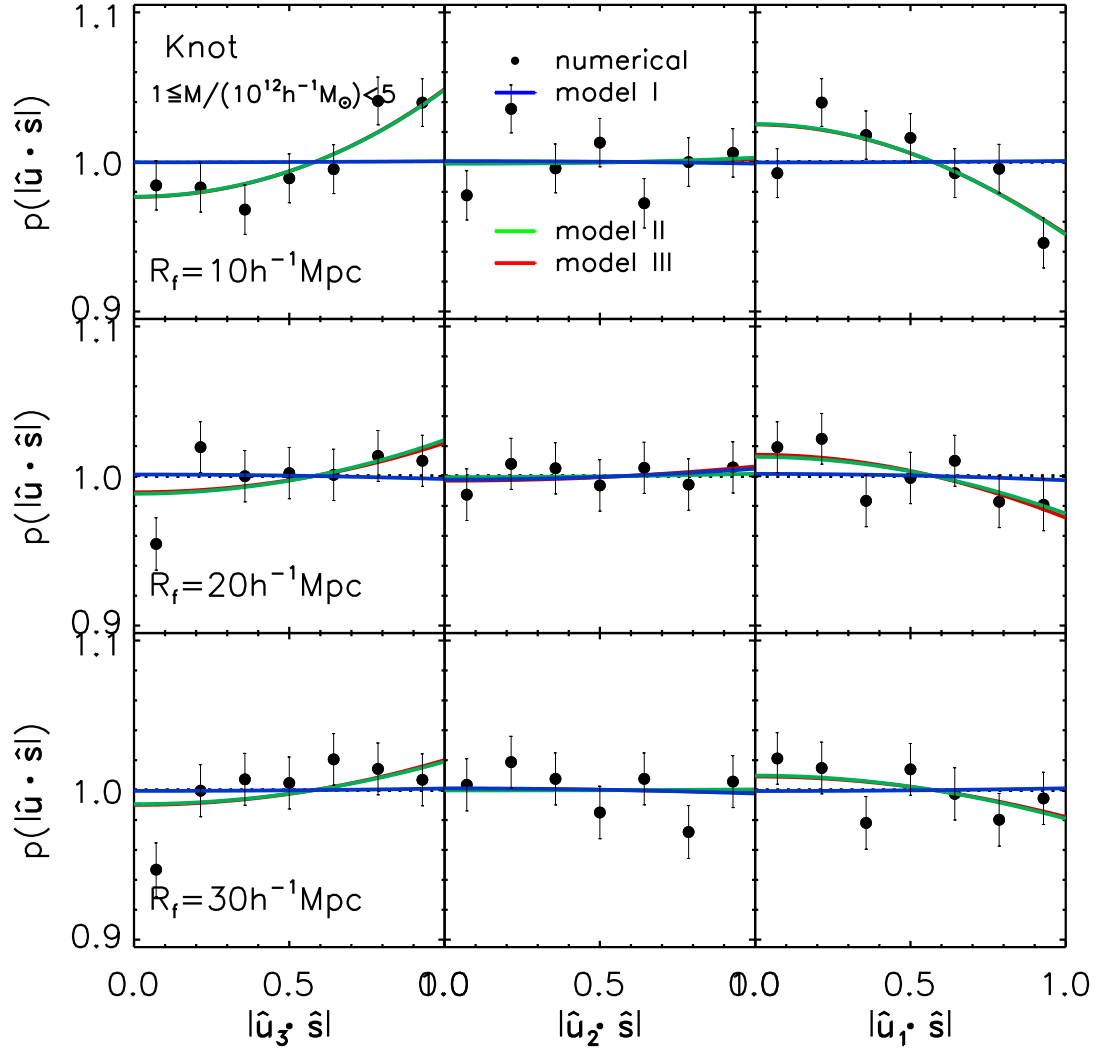


Fig. 25.— Same as Figure 17 but with only those galactic halos located in the knot environments.

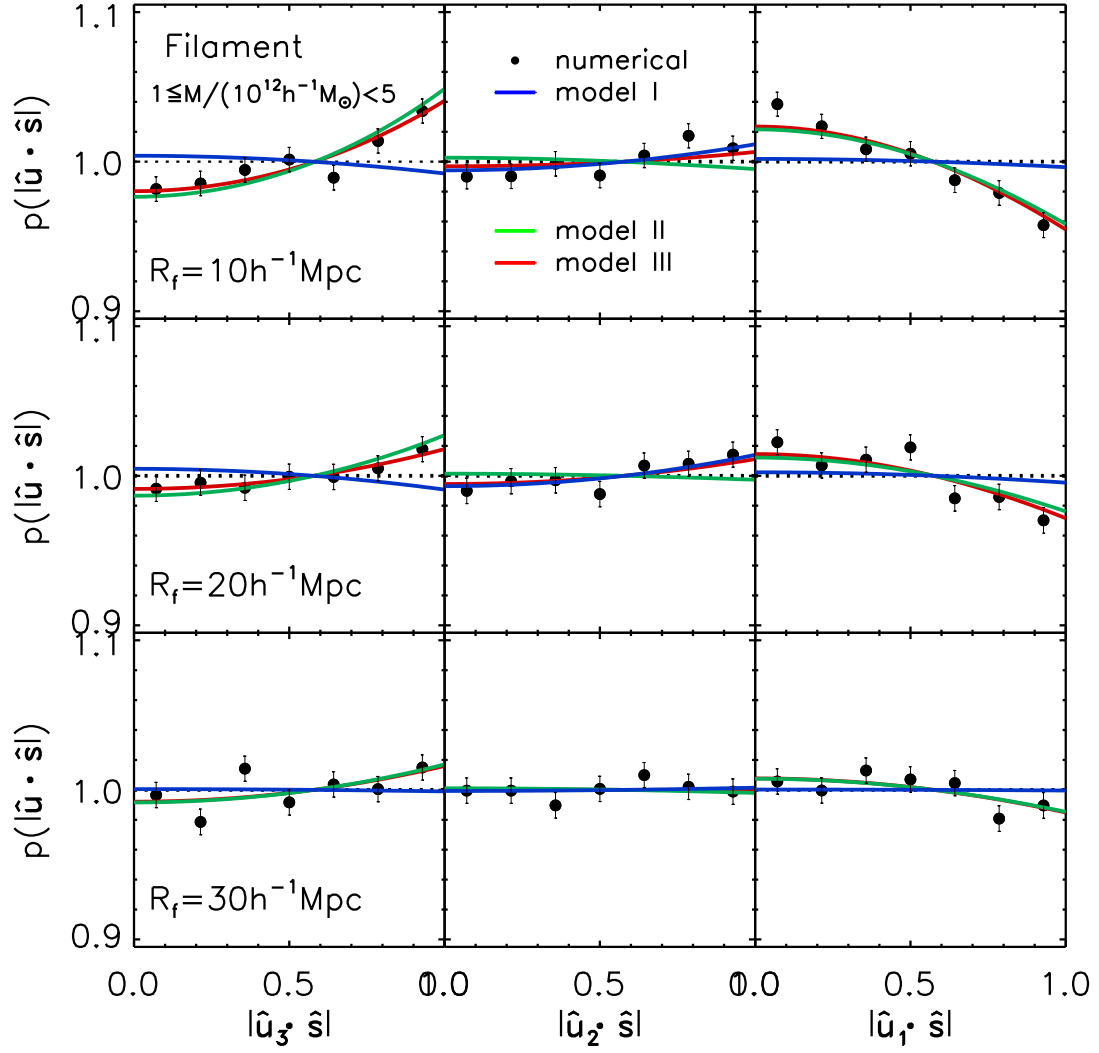


Fig. 26.— Same as Figure 17 but with only those galactic halos located in the filament environments where $\lambda_1 > \lambda_2 > 0 > \lambda_3$.

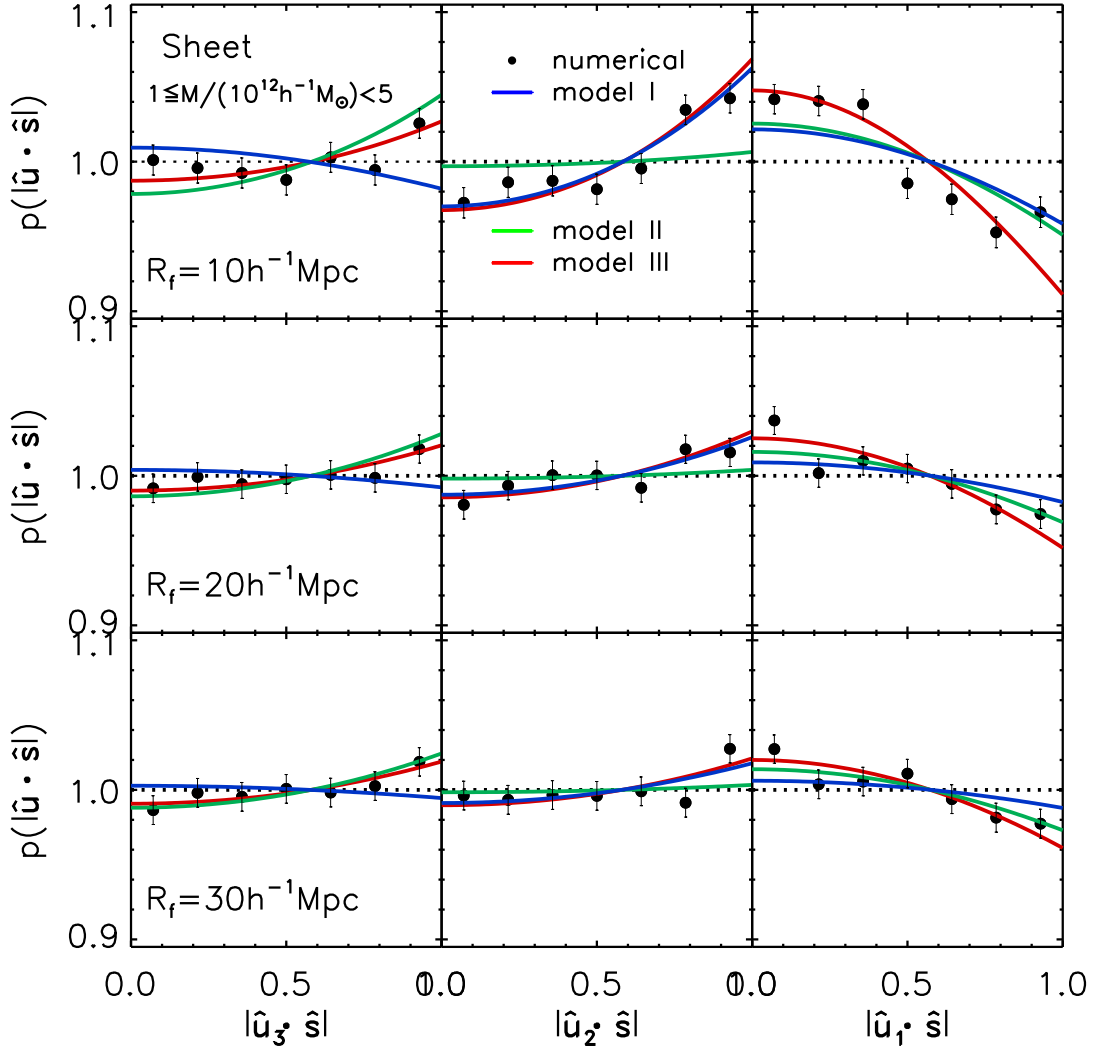


Fig. 27.— Same as Figure 17 but with only those galactic halos located in the sheet environments where $\lambda_1 > 0 > \lambda_2 > \lambda_3$.

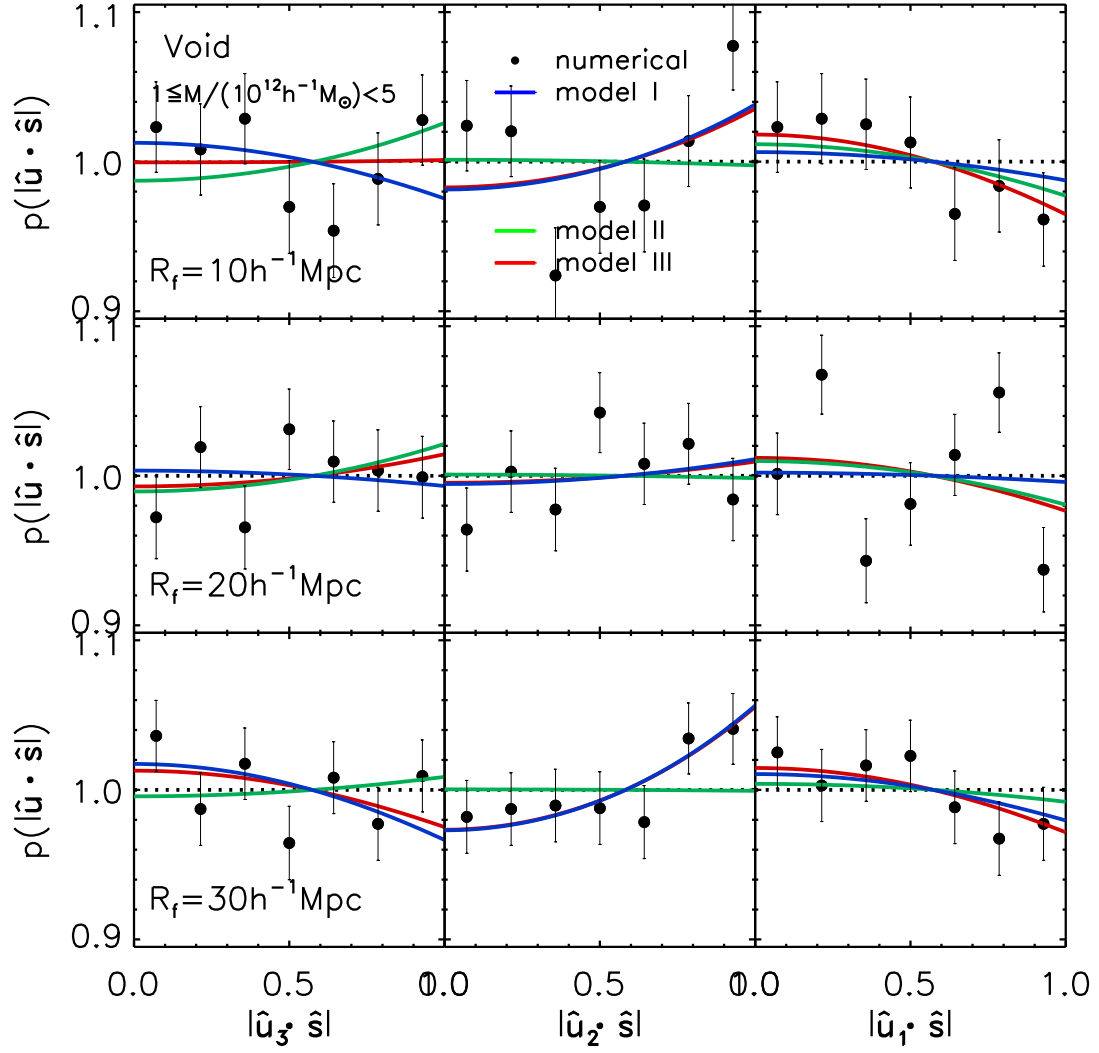


Fig. 28.— Same as Figure 17 but with only those galactic halos located in the void environments where $0 > \lambda_1 > \lambda_2 > \lambda_3$.